Transverse Acoustic Actuation of Ni–Mn–Ga Single Crystals

by

Jesse Matthew Simon

Submitted to the Department of Aeronautics and Astronautics
in partial fulfillment of the requirements for the degree of

Master of Science

at the

MASSACHUSETTS INSTITUTE OF TECHNOLOGY

February 2007

Author ..... February 12, 2007

Certified by .....
Steven R. Hall
Professor of Aeronautics and Astronautics
MacVicar Faculty Fellow
Thesis Supervisor

Accepted by .....
Jaime Peraire
Chairman, Department Committee on Graduate Students

Transverse Acoustic Actuation of Ni–Mn–Ga Single Crystals

by

Jesse Matthew Simon

Submitted to the Department of Aeronautics and Astronautics
on February 12, 2007, in partial fulfillment of the
requirements for the degree of
Master of Science

Abstract

Two methods for the transverse acoustic actuation of {110}-cut Ni–Mn–Ga single crystals are discussed. In this actuation mode, crystals are used that have the {110}-type twinning planes parallel to the base of the crystal. The first method employs two 33-mode piezoelectric stacks, mounted at 45 deg to the base of a single crystal, to produce a shear stress on the 110 planes. The second method utilizes a single 15-mode piezoelectric stack, normally incident to the crystal base, to generate shear pulses directly. Both methods are capable of producing acoustic actuation.

Due to the small size of the 15-mode stack, and the need to prestress the 33-mode stacks to prevent them from failing due to tensile stresses, the single stack actuator was chosen for further investigation. Engineering strains of up to $\gamma = 0.12$, the theoretical maximum for Ni–Mn–Ga, have been realized in the single stack configuration. Actuating over a smaller range, the actuator produced 5% strain in as little as 2.5 s, at a pulse frequency of 100 Hz, with over 3% occurring within the first second. Actuation against a load was also investigated. The blocking stress was found to be around 0.14 MPa, indicating that the acoustic stress exceeded the twinning stress by approximately this amount. The maximum output energy density of the actuator was approximately 4000 J/m^3, for an opposing stress of 0.08 MPa. Given the electrical power consumption of the actuator, which is around 375 mW at 100 Hz, the overall actuator efficiency is approximately 4×10^{-4}.

Recent results for both methods are presented, including new evidence of a viscous loss mechanism that governs the strain rate of the crystal. An increase in the displacement per pulse with frequency is observed, indicating that the inertia of the moving portion of the crystal may cause it to deform even after the pulse has passed.

Thesis Supervisor: Steven R. Hall
Title: Professor of Aeronautics and Astronautics and MacVicar Faculty Fellow

Acknowledgments

First, I would like to thank my advisor, Prof. Steven Hall, without whose support and patience I would not be where I am today. I am truly grateful to a number of people at MIT who have taught me as much as any of my professors, and who deserve a great deal of credit for my successful completion of this thesis: Bob O'Handley, who has provided so much guidance and support that I forget I'm not one of his advisees; David Bono, who has taught me a great deal, and whose genuine excitement about every project he lays his hand on is contagious; and Fred Cote in the Edgerton Student Shop, now retired, who prevented me from becoming the kind of engineer that doesn't know a collet from an endmill. I would also like to thank my labmate Ratchatee Techapiesancharoenkij, and former labmates Marc Richard, Jorge Feuchtwanger and Brad Peterson, for their invaluable assistance in all manner of things.

I also owe an enormous debt of gratitude to my family, who have believed in me and been there for me throughout. Now, at last, I've earned the name "Mohandas." Thanks too to my friends, who've borne with me, even though I haven't been much fun over the past couple of years, for constantly reminding me that there's much more to life than numbers.

Last, but certainly not least, I would like to thank Marie Stuppard, surrogate mother to all Aero-Astro students, without whose constant support and encouragement I would surely have foundered long ago. Merci mille fois, Marie!

This work was sponsored by the Office of Naval Research, grant number ONR-MURI N00014-01-10758, monitored by Dr. Roshdy Barsoum and Dr. Jan Lindberg.

Contents

Chapter 1

Introduction

Ni–Mn–Ga is an active material that has attracted a great deal of attention over the past 10 years. It belongs to a class of materials known as ferromagnetic shape memory alloys (FSMAs), a subset of shape memory alloys that are ferromagnetic in the martensite phase, and thus can change their structure in response to an applied magnetic field. Magnetic actuation of these materials has been investigated extensively (e.g., [35, 27, 25, 10, 20, 16]), however this phenomenon is not the focus of the work in this thesis. Rather, the material is chosen due to its ability to deform by twin boundary motion, and the extremely low stress necessary to initiate this mechanism. Using piezoelectric stack actuators, it is possible to generate an acoustic stress that exceeds this threshold "twinning stress", and by generating highly asymmetric acoustic pulses, twin boundary motion may be induced in one direction but not the other. In this way, a permanent, or plastic, strain may be obtained, that is preserved after the pulse has passed. By reversing the sign of the pulse, it is possible to undo this deformation exactly. In this chapter, a brief outline is given to show where this alloy fits in the spectrum of known active materials, and the potential and limitations of this material for incorporation into practical actuator devices.

1.1 Active Materials

An active material is one which can produce mechanical work in response to an applied stimulus. Examples range from thermally activated metallic alloys to muscle tissue, which

responds to electrical signals. Similarly, a piezoelectric material is one that produces stress or strain (from Greek *'piezein'*, meaning to press or squeeze) in response to an electrical signal, or vice versa. Examples of this type of material include quartz (SiO_2) and many piezoceramics, including lead zirconate titanate ($Pb[Zr_xTi_{1-x}]O_3$). Other active materials, known as magnetostrictors, will produce stress or strain under an applied magnetic field. Examples of these materials include pure nickel, and Terfenol-D ($Tb_{0.3}Dy_{0.7}Fe_2$). Conventional shape memory alloys, on the other hand, deform by means of a thermally induced phase change.

1.1.1 Shape memory alloys (SMAs)

The first shape memory alloy was discovered in 1962 by scientists at the Naval Ordnance Laboratories, who were investigating the properties of nickel-titanium alloys. The resulting material became known as Nitinol (Nickel Titanium Naval Ordnance Laboratories), and is today perhaps the best known shape memory alloy. The shape memory effect in this material comes from a diffusionless transformation between a high temperature phase, in which the lattice structure is usually cubic, to a low temperature phase in which one or two of the lattice constants becomes shorter, giving a lower-symmetry structure. The high and low temperature phases are known as austenite and martensite, respectively. A tetragonal martensite has a total of three martensitic variants, distinguished by the crystallographic direction of their shortest axis. The boundaries between these variants are called twin boundaries.

When a a compressive stress is applied in a particular direction, the variant with its shortest axis most closely aligned with that direction will tend to grow at the expense of the others, through the motion of the twin boundaries, to give a configuration that minimizes the elastic energy in the material. This mode of deformation can result in strains of up to 10%, which are not recovered when the stress is removed. By heating the crystal back into the austenite phase, however, this deformation is reversed completely. Without additional treatment, cooling the crystal back into its low temperature phase will not cause it to return to its deformed shape; this type of actuation is known as one-way actuation.

Figure 1-1 shows the deformation vs. temperature characteristic of a single crystal of a conventional SMA undergoing thermal cycling. In Figure 1-1(a), the fraction of the crystal

that is in the martensitic phase is plotted against the temperature. Suppose the crystal begins in the high temperature, austenite phase. As the temperature falls below the martensite start temperature, T_m^s, the crystal begins the transformation to martensite. By the time the temperature falls below the martensite finish temperature, T_m^f, it has transformed completely to the low-temperature phase. Figure 1-1(b) shows the result when the crystal is allowed to cool without an applied load. The two variants shown adopt a self-accomodating structure, with variant 1 having its short axis nearly horizontal, and variant 2 with it nearly vertical. To the right of the figure, the change in lattice constants is illustrated, with the single cubic dimension a_0 being transformed to two longer a-axes (one of which is into the plane of the page), and a shorter c-axis. In Figure1-1(c), a compressive stress σ is applied in the martensitic state. In order to minimize its strain energy, the variant with its short axis most closely aligned with the stress will be favored. In this case, variant 2 is favored and will therefore grow at the expense of variant 1, by the motion of twin boundaries. The mechanism by which twin boundary motion occurs will be explained in greater depth in Chapter 2. When the compressed crystal in Figure 1-1(c) is heated above the austenite finish temperature (T_a^f in Figure 1-1(a)), it regains its cubic lattice structure and the deformation is undone. Finally, when the crystal is cooled again into the martensite phase, it does not regain the compressed, single variant structure, unless a compressive stress is applied.

Two-way actuation can also be accomplished with these materials, by training the crystal to give it a preferred, low temperature shape. To this end, the crystal is cycled thermally, repeatedly, each time being allowed to cool under the application of a biasing stress. The effect of deforming the crystal repeatedly is to move plastic and twinning dislocations into stable configurations. Heating the material slightly above the austenite finish temperature does not erase its "memory" of this low-temperature state, which the crystal will seek to reestablish each time it is cooled.

Recently, Nitinol has also been of interest due to its superelastic properties. Superelasticity arises from the fact that, even at temperatures above T_m^s, it is possible to effect the stress induced nucleation of the martensitic variant. Objects made with Nitinol, such as eyeglass frames, can therefore be subjected to large strains (which induce the martensite phase), and spring back to their original shape when the stress is removed (as the material transforms

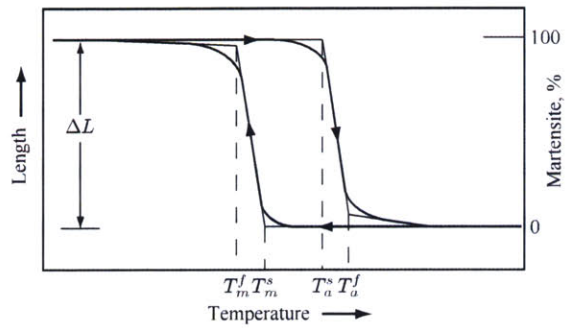

(a)

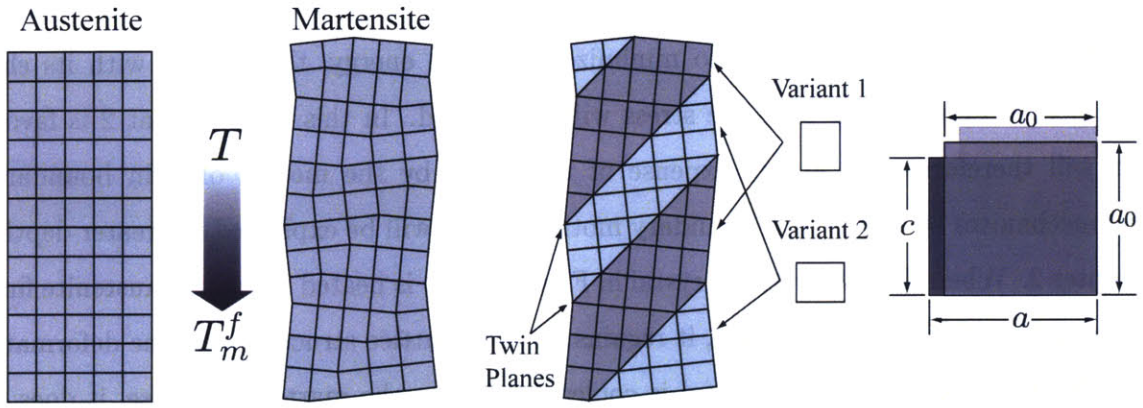

(b)

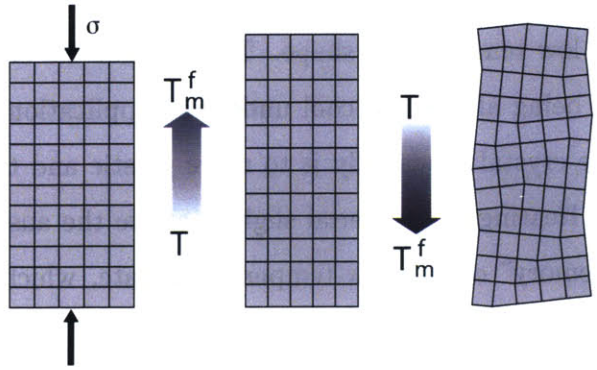

(c)

Figure 1-1: A conventional shape memory alloy (a) undergoing thermal cycling between austenite and martensite phases, (b) cooling to martensite without an applied stress, and (c) being compressed to a single-variant state, reheated to austenite, and left to cool without applying any stress. Adapted from [3].

back to austenite).

1.1.2 Ferromagnetic Shape Memory Alloys (FSMAs)

FSMAs are a type of shape memory alloy which, in their martensitic phase, can produce a stress or strain in reponse to an applied magnetic field. The strains produced by these materials are much greater than those from magnetostrictors, and can be as large as 10% in orthorhombic Ni–Mn–Ga [32]. The blocking stresses these materials can support, though, are generally quite low — on the order of 1 MPa, which gives them an energy density on the order of $10^3 - 10^4$ J/m^3, similar to that of piezoceramics, which can produce much larger stresses but much smaller strains.

Figure 1-2 shows an alternative expression of the actuation characteristics of FSMAs, by plotting the specific actuation stress against the actuation strain. The specific actuation stress, σ_s, is defined as

$$\sigma_s = \frac{\sigma}{\rho}, \tag{1.1}$$

where σ is the actuation stress and ρ the mass density, and has units of J/kg. The product of the specific stress and strain gives the specific energy density. As the figure shows, FSMAs produce similar strains at higher specific stresses than electromagnetics, while compared to piezoelectrics they produce lower specific stresses and much larger strains. When the specific work is considered, FSMAs are found to outperform electromagnetic devices, (e.g., solenoids), as well as piezoelectrics.

The maximum actuation frequency that can be achieved with FSMAs appears to be limited to approximately 2 kHz [17]. If the specific work is plotted against the bandwidth, the result is as shown in Figure 1-3. It should be noted that bandwidth of an actuator is also a function of its size, and the force with which it is driven; the plot represents the frequency range within which common devices of each type operate. In typical applications, it may be seen from Figure 1-3 that piezoelectrics allow much higher frequency actuation than FSMAs, which are similar to electromagnetic devices in their bandwidth. Again, FSMAs outperform both of these technologies in terms of the specific work they can perform.

With an appropriate actuation mechanism, then, FSMAs may be suitable for many ap-

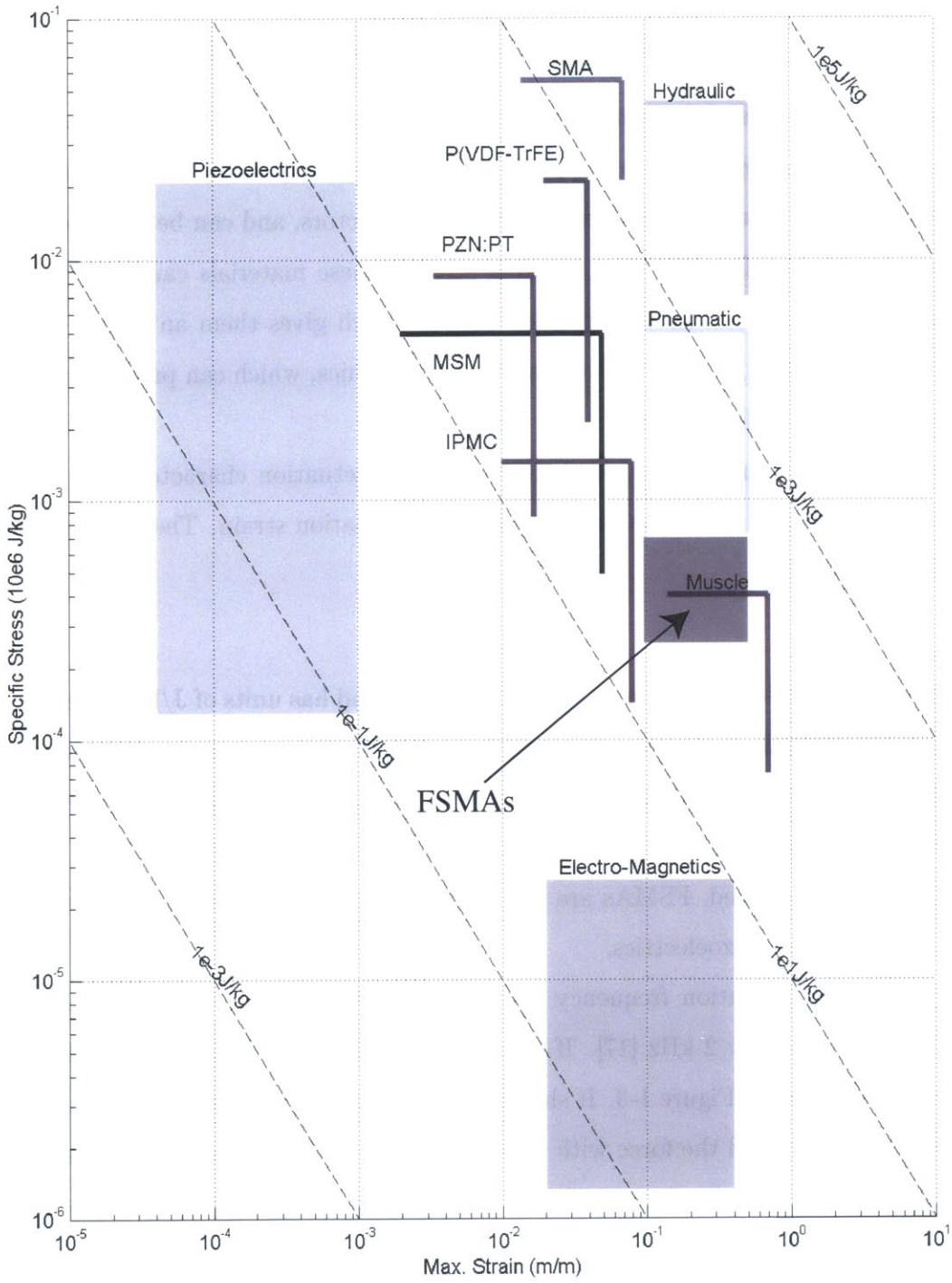

Figure 1-2: Approximate representation of the specific actuation stress vs. strain for FSMAs, compared to other methods of actuation. Adapted from [11].

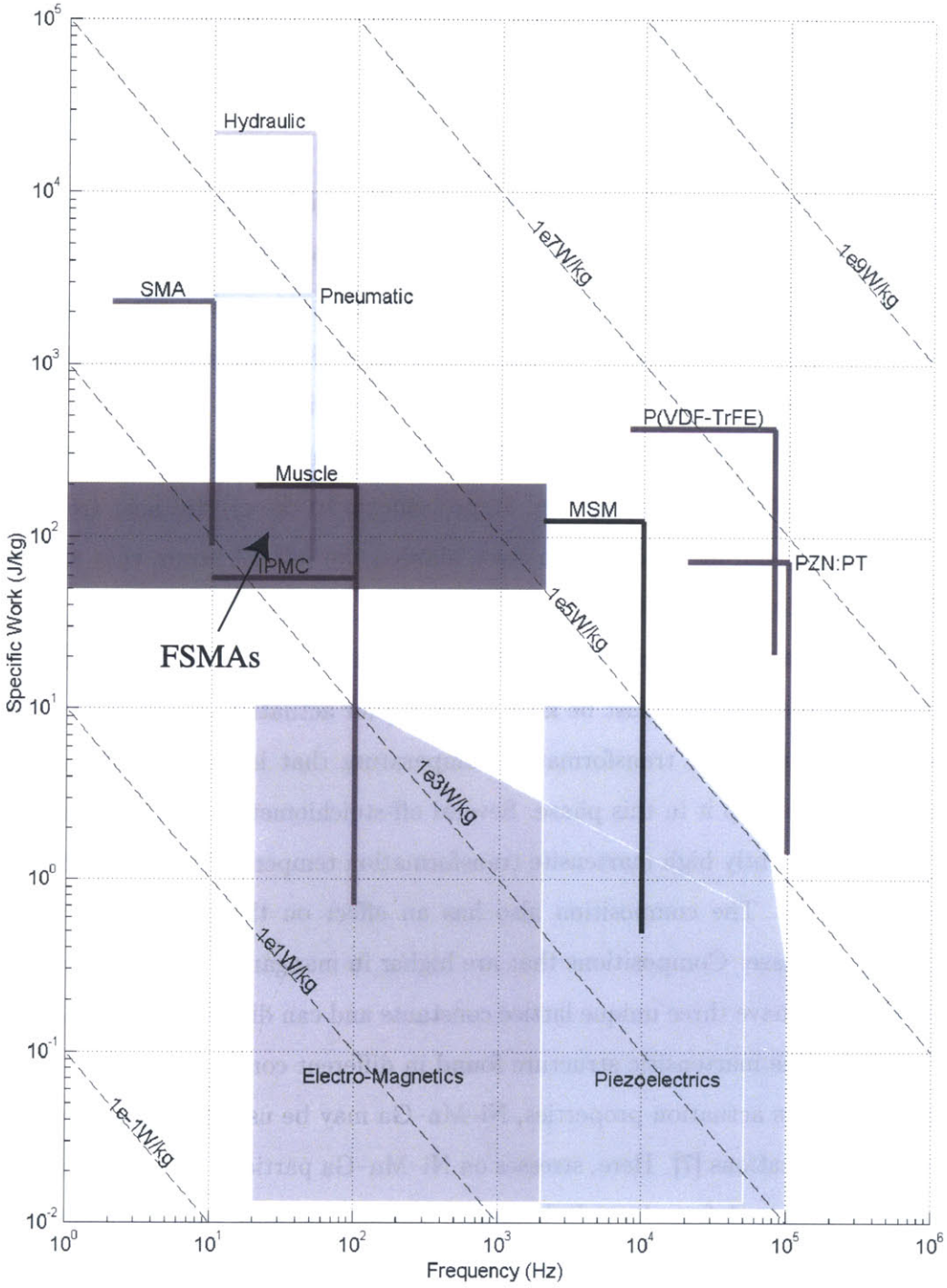

Figure 1-3: Specific work of FSMA devices vs. actuation frequency, compared to other methods of actuation. Adapted from [11].

plications requiring larger strains than can be achieved with piezoelectrics, at modest frequencies, while providing more stress per mass than an electromagnetic device.

1.2 Ni–Mn–Ga

The Ni–Mn–Ga system first attracted interest as a potential material that could exhibit a magnetically-controlled shape memory effect, to produce appreciable strains at a constant temperature. Ullakko *et al.* were the first to obtain significant strains using only a rotating magnetic field. The resulting strain of 0.19% for a field of 8 kOe was an order of magnitude greater than the magnetostriction exhibited by the material [35]. The strain was limited by the small number of mobile twin boundaries in the sample, and the lack of training to promote a single active twinning system. Improvements to the crystal heat treatment and mechanical training during cooling have since allowed the full 6% strain that this material can develop to be exploited. [24, 25]

The shape memory effect in Ni Mn Ga arises from a transformation between martensitic variants, so the material must be kept below T_m^f for actuation to occur. Stoichiometric Ni_2MnGa has a martensite transformation temperature that is below room temperature, requiring cooling to keep it in this phase. Several off-stoichiometric compositions have been found to have sufficiently high martensite transformation temperatures to permit room temperature actuation. The composition also has an effect on the crystal structure of the low-temperature phase. Compositions that are higher in manganese can form orthorhombic martensites, which have three unique lattice constants and can display up to 10% strain [32]. Figure 1-4 shows the martensitic structure found in different composition fields.

In addition to its actuation properties, Ni–Mn–Ga may be used in composites for vibration damping applications [7]. Here, stresses on Ni–Mn–Ga particles embedded in a polymer matrix causes them to deform by twin boundary motion. Because twin boundary motion is a dissipative process, it has a damping effect on the vibration.

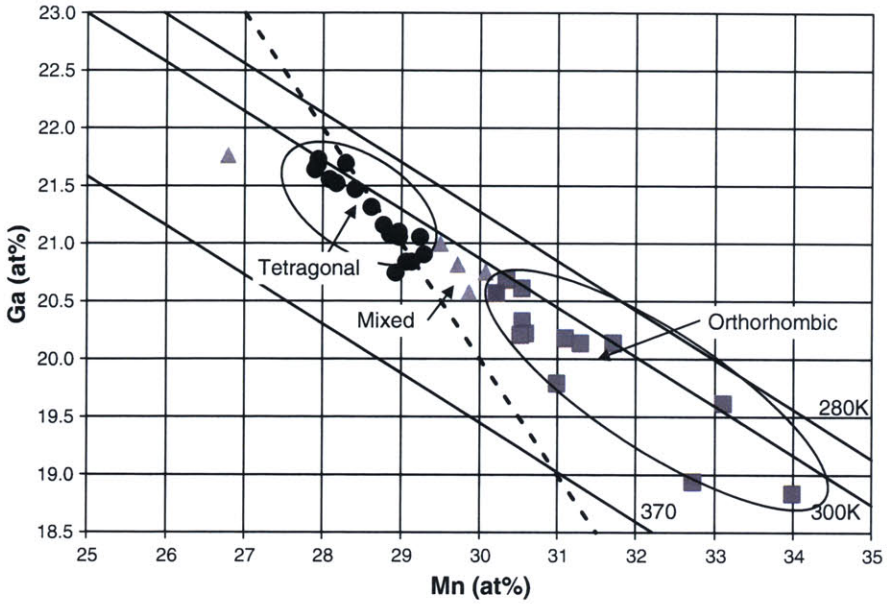

Figure 1-4: The composition of the alloy can affect the crystal structure of the martensite phase; alloys richer in gallium tend to form tetragonal martensites, while those that are richer in manganese can adopt an orthorhombic structure. From [29].

1.2.1 Magnetic Actuation

The ferromagnetic nature of Ni–Mn–Ga has made it particularly interesting for magnetically driven applications. The magnetic easy axis (i.e., the preferred direction of the magnetization vector, **M**, in zero field) is the c-axis in tetragonal Ni–Mn–Ga. Thus, when a magnetic field is applied the energy is lowest for variants with a c-axis parallel to the field. Equivalently, the short, c-axis of the martensitic phase will tend to line up with an applied magnetic field, and constraining a crystal from rotating will generate a torque that can be resolved as a shear stress along the shear plane. If this stress exceeds the twinning stress, τ_0, of the material, and the twin boundaries are mobile, the crystal will then transform to the variant with its c-axis best aligned with the field.

O'Handley [26] developed a model relating the driving force for twin boundary motion to the applied magnetic field. The model presents two limiting cases for a magnetic shape memory alloy: first, where the magnetocrystalline anisotropy, K_u, is very weak compared to the Zeeman or magnetization energy, U_Z, and second, where the reverse is true.

For the weak anisotropy case, the magnetization within a martensitic variant can be rotated away from its direction of easy magnetization, which is parallel to the c-axis. The driving force for the motion of a twin boundary, in this case, results from the difference in anisotropy energy between the variants on either side of it, which may be expressed as

$$P = K_u \sin^2\phi, \tag{1.2}$$

where ϕ is the angle between the c-axes of the two variants.

In the case of very strong anisotropy, where the magnetization cannot be rotated away from the easy axis, the contribution from the Zeeman energy is much more important. The difference in Zeeman energy between the two variants is given by

$$U_Z = -(\mathbf{M}_1 - \mathbf{M}_2) \cdot \mathbf{H}, \tag{1.3}$$

where $\mathbf{M}_i$ is the direction of magnetization in variant i, and $\mathbf{H}$ is the applied magnetic field.

In reality, a material will generally fall between these limits. In this case, the driving force is the result of the difference in total free energy between the variants, which will contain contibutions from both the Zeeman energy and the anisotropy energy.

Marioni [15] related the difference in free energy between variants to the equivalent stress needed to move the twin boundary. The difference in the Gibbs free energy, Δg, between two adjacent variants is given by

$$\Delta g = \begin{cases} -K_u(2\eta - \eta^2), & \eta \leq 1 \\ -K_u, & n > 1 \end{cases}, \tag{1.4}$$

where

$$\eta = \frac{H}{H_a} = \frac{\mu_0 M_s H}{2K_u} \tag{1.5}$$

is the non-dimensional field strength [26, 24].

The equivalent magnetic shear stress, τ_m, may be related to the free energy difference as

$$\tau_m = \frac{\Delta g}{\gamma_0}, \tag{1.6}$$

where γ_0 is the twinning strain. For the case where $\eta > 1$, the maximum free energy difference is the magnetocrystalline anisotropy, K_u, which results in a maximum twinning stress, or blocking stress, of approximately 3 MPa, and an energy density of $1.9 \times 10^5\,\mathrm{J/m^3}$.

Marioni [16, 15] found that, in fact, the twinning stress varies for different twin boundaries. Using sub-millisecond magnetic field pulses, the stochastic nature of twin boundary motion was observed and attributed to the presence of defects of varying strength. Expressed in terms of the anisotropy, these defects were found to have strengths that were distributed broadly up to approximately $0.7\,K_u$, with a peak near $0.56\,K_u$, which is equivalent to approximately 1.7 MPa.

Henry [9, 10] studied cyclic magnetic actuation over a range of frequencies, against prestresses ranging from 0.3 MPa to 2.8 MPa. Here the magnetic field favored one martensitic variant, while an applied compressive stress favored the other. Thus, by generating a sinusoidal field, bidirectional actuation could be achieved, using the prestress as the reset stress when the field falls below the threshold twinning field. A set of results corresponding to a prestress of 1.7 MPa, which was found to be the optimal value, are shown in Figure 1-5. The decreasing performance of the actuator at frequencies above 300 Hz was ascribed to the inductive reactance of the magnet, and not to an inherent property of the material.

More recently, Müllner *et al.* [23] have studied cyclic actuation in single crystals of Ni–Mn–Ga that have been either subjected to a thermomechanical treatment to induce a single-variant initial state, and that have been left to cool from the cubic phase in the absence of a biasing stress, leaving a poly-variant state. It was found that the single-variant crystals realized the full shear strain expected for the material, which was 10% for the orthorhombic composition used. However, the crystals failed by fracture after a few thousand cycles. Conversely, those that had a poly-variant structure exhibited two orders of magnitude less strain, but did not fail even after 10^7 cycles. An example of these actuation data is shown in Figure 1-6.

1.2.2 Acoustically Assisted Magnetic Actuation

Peterson *et al.* [28] developed a method to improve magnetic actuation performance, by propagating longitudinal acoustic stress waves into a single crystal of Ni–Mn–Ga, using

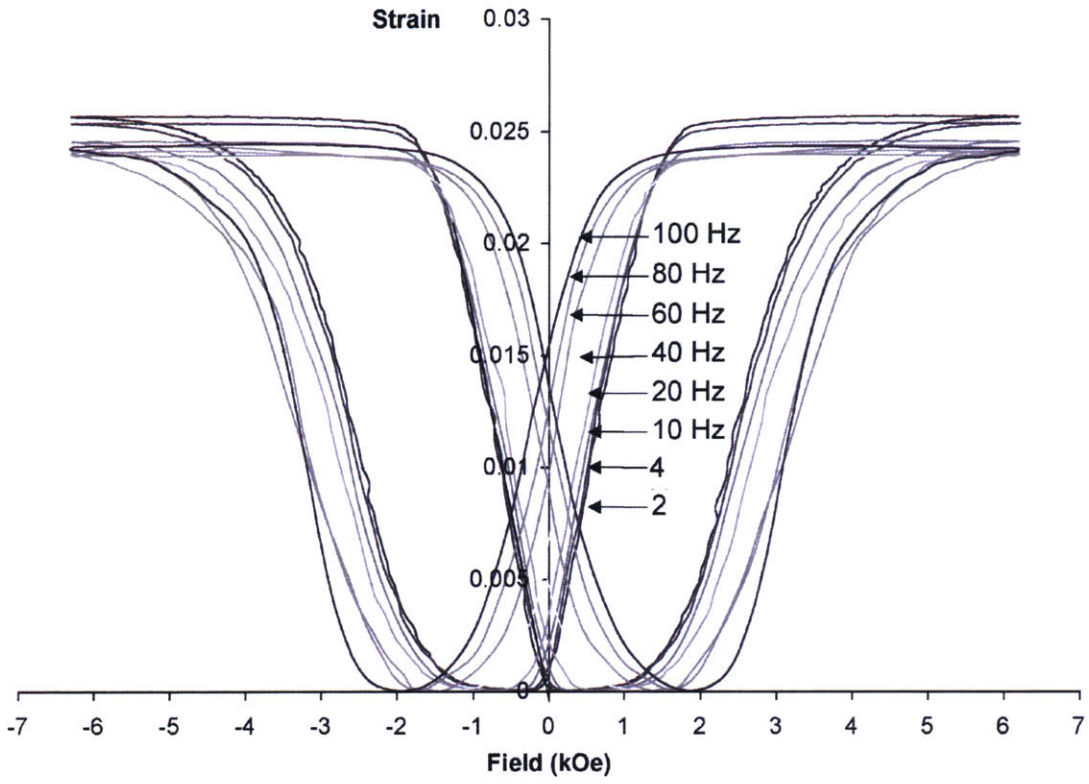

Figure 1-5: Cyclic magnetic actuation of a Ni–Mn–Ga single crystal against prestress of 1.7 MPa, for a range of frequencies. From Henry [9].

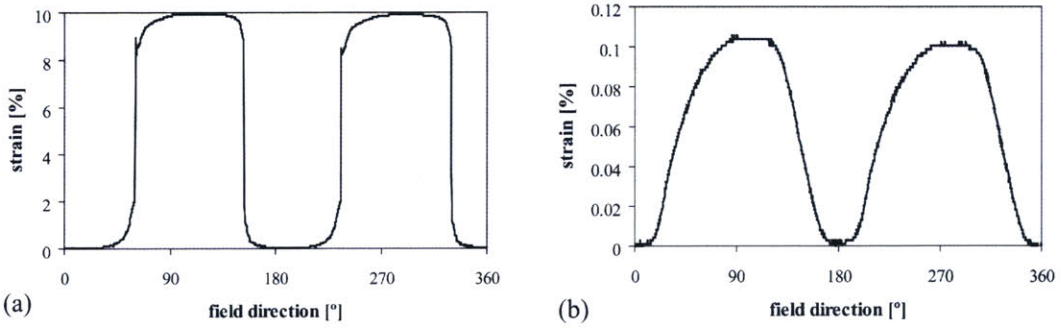

Figure 1-6: Cyclic magnetic actuation of a single crystal of Ni–Mn–Ga with an orthorhombic martensitic structure, which began in (a) a single-variant state and (b) a poly-variant state. From [23].

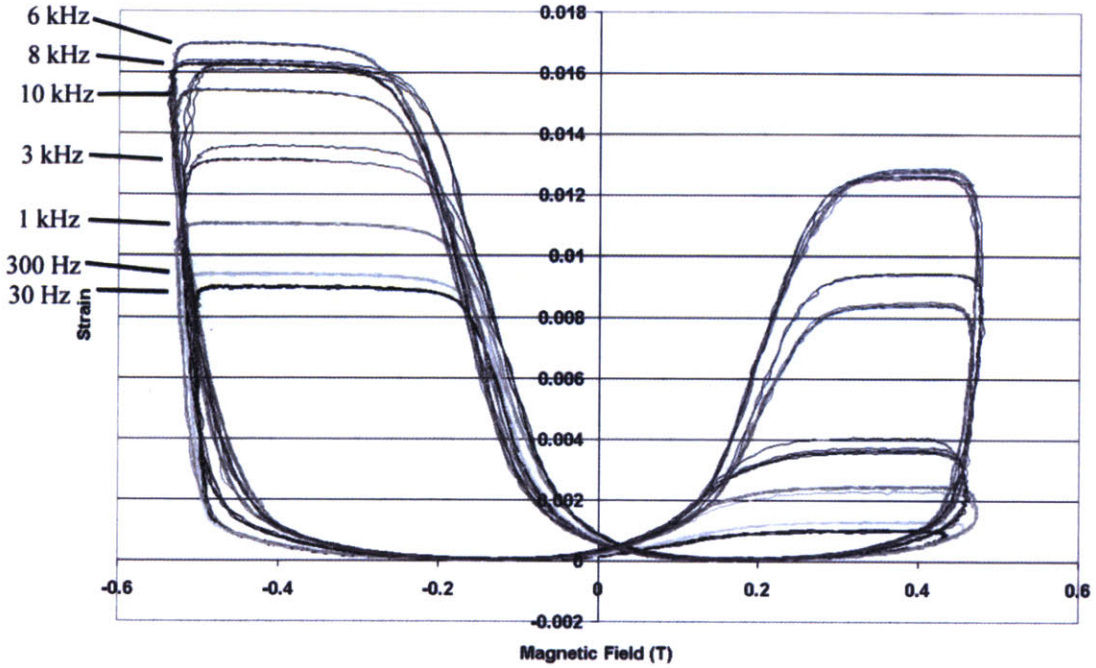

Figure 1-7: Acoustically assisted, cyclic magnetic actuation with an added acoustic stress, shown for a range of acoustic frequencies. From [28].

a piezoelectric stack actuator, while it was subjected to an oscillating magnetic field and mechanical prestress. Although the stress waves were sinusoidal and did not inherently bias the crystal in favor of a particular variant, the additional acoustic energy supplied was shown to both increase the total strain obtained, and to decrease the threshold magnetic field necessary to initiate twin boundary motion. The performance was shown to increase with the frequency of the stress waves, up to a limit of about 6 kHz. Figure 1-7 shows some typical results of these experiments, for magnetic actuation with an added acoustic signal of varying frequency.

1.2.3 Acoustic Actuation

In the work of Chambers *et al.* [4] and Chambers [3], the possibility of inducing twin boundary motion by a purely acoustic means was first proposed. In order for an acoustic signal to initiate twin boundary motion, it must produce a stress of sufficient magnitude, and that stress must be biased so that it exceeds the twinning stress in one actuation direction but

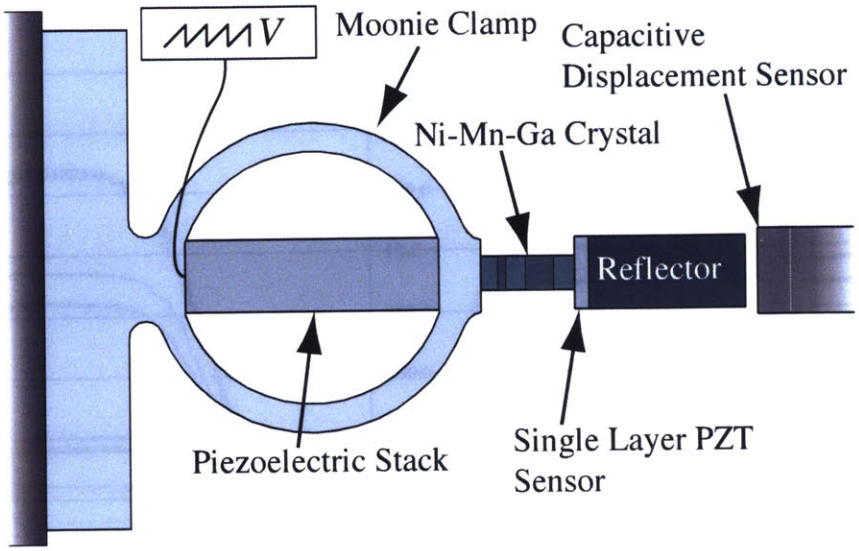

Figure 1-8: Apparatus used by Chambers [3] for the acoustic actuation of Ni–Mn–Ga single crystals.

not in the other. One method of meeting these requirements was found to be the propagation of highly asymmetric, sawtooth-shaped stress pulses into the crystal. Reversing the sign of these pulses reversed the actuation direction.

A schematic of the apparatus is shown in Figure 1-8. Because the longitudinal, or 33-mode piezoelectric stack employed in Chambers' experiment could not withstand any tensile stresses, it was necessary to apply a compressive prestress to the stack using a "Moonie" clamp. With this actuator, strains of 1% were obtained in less than 1 s, while in 30 s nearly 3% was obtained. Figure 1-9 shows some typical bidirectional actuation data when no longitudinal prestress was applied to the crystal. The maximum output energy density, obtained with a compressive prestress of 0.1 MPa, was found to be approximately 1000 J/m^3.

1.3 Motivation for this Work

Building upon the Chambers' work, a more efficient design for acoustic actuation was sought. The single crystals used in the first acoustic actuators [4, 3] were oriented such that each face was a {100} plane, referred to here as {100}-cut crystals. In this orientation, the twinning

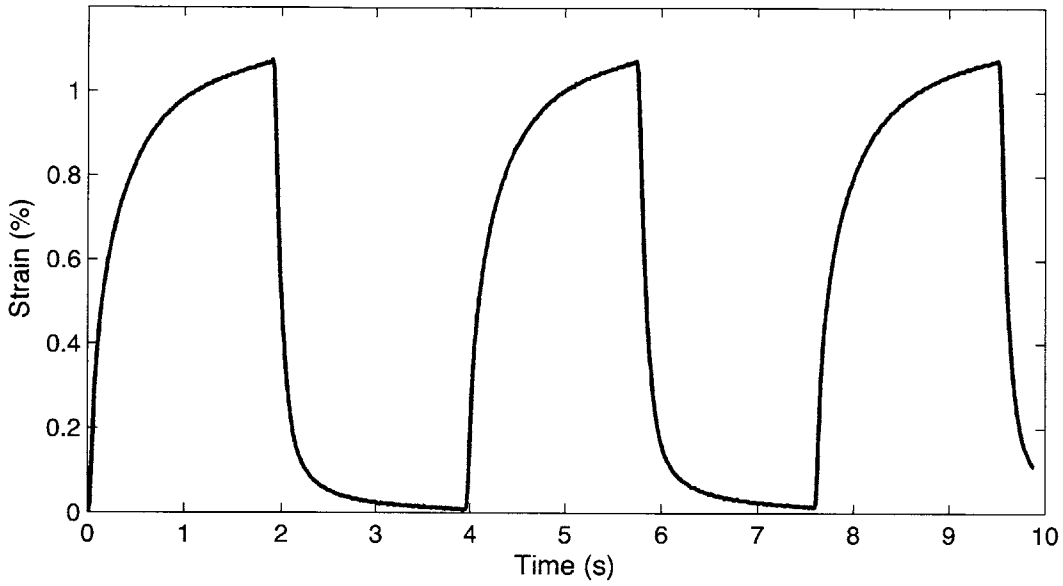

Figure 1-9: Bidirectional acoustic actuation data in the absence of a load. From [4].

planes lie at approximately 45 deg to the crystal's long axis. Crystals of this orientation are often chosen for actuation, because variant formation during cooling, and twin boundary motion can be induced by a longitudinal stress (or field). An axial stress will be parallel to a potential orientation for the c-axis, and will favor the variant with its c-axis in that direction. Equivalently, because an axial stress resolves to a shear stress along the twinning plane, it can initiate twin boundary motion if the twinning stress is exceeded.

There are disadvantages to this orientation, however. First, because the strain direction is parallel to the twin boundary, the tip of the crystal does not move longitudinally, but rather at an angle of about 45 deg to the normal of the end face. The resulting motion can be difficult to exploit fully, and in previous acoustic actuators [4, 3] only the longitudinal component was considered. Second, when the end faces of a {100}-cut crystal are bonded to the stack-clamp assembly on one end and a reflector on the other, twin boundaries cannot move past the corner of the crystal. When these twin boundaries become pinned, there are two triangular regions at either end that do not actuate. Finally, due to the need to maintain a compressive stress on the piesoelectric stack, a clamp or other device must be used. By adding to the overall size and mass of the actuator, the clamp reduces its effective energy

density. Further, the clamp leads to an asymmetric response in the two actuation directions, since during tensile pulses the end of the stack is retracted more quickly than the clamp can respond.

Motivated by an effort to improve the efficiency of longitudinal actuation, this thesis presents work on an alternative mode of acoustic actuation. Here, a different crystal orientation was used, with the twinning planes normal to the length of the crystal. Twin boundary motion in this orientation produces a transverse displacement of one end of the crystal with respect to the other. In order to generate the transverse, or bulk shear waves, two configurations were tested. The first employed two longitudinal, or 33-mode piezoelectric stacks, oriented at 45 deg to the base of the crystal, to generate the shear stress indirectly. In the second apparatus, a single shear or 15-mode piezoelectric stack was used, to produce normally-incident shear waves at the base of the crystal. Both methods allowed the clamp to be eliminated completely, and the latter provided a significant reduction in the overall size of the actuator. In addition, since both piezoelectric configurations should produce an equal peak acoustic stress in either direction, the reponse of the actuator was also expected to be symmetrical.

Experiments on these devices were carried out to determine whether this mode of actuation would indeed be practical. In addition, by examining the effect of the shape and frequency of the acoustic stress pulses, a better understanding of the underlying mechanisms was sought. This work is a part of ongoing investigations to characterize this new class of materials, and to look for suitable applications of devices containing them.

In Chapter 2, some relevant aspects of the theoretical background to this work are explained. Chapter 3 describes the experimental apparatus and procedure that were employed. The results of these experiments are presented in Chapter 4, together with a discussion of their significance. Finally, conclusions drawn from the experiments, and suggestions for future work, are discussed in Chapter 5.

Chapter 2

Background

This chapter outlines the theoretical background underlying the experimental work done in this thesis. Section 2.1 describes the structure and properties of both stoichiometric Ni_2MnGa, and the off-stoichiometric compositions employed in these experiments. Section 2.2 explores the shape memory effect exhibited by these alloys, and the principles behind both magnetic and mechanical action. Finally, Section 2.3 outlines the theory behind the acoustic method of actuation studied here.

2.1 Properties of Ni–Mn–Ga

2.1.1 Stoichiometric Ni_2MnGa

Stoichiometric Ni_2MnGa is an alloy that forms an intermetallic compound, rather than a solid solution of elements, meaning that the different species of atom adopt an ordered lattice structure. At room temperature, the stoichiometric composition is in the austenite phase, in which all atoms occupy sites of a body-centered cubic lattice. The unit cell, shown in Figure 2-1(a), has a Heusler or $L2_1$ structure, $Fm\bar{3}m$ symmetry, and a lattice constant of $a = 5.822\,\text{Å}$ [35, 31]. Upon heating above approximately 800 °C, the Mn and Ga atoms become disordered, giving rise to a B2 structure with $Pm\bar{3}m$ symmetry, shown in Figure 2-1(b). [31]

Below the martensite transformation temperature, which is approximately 276 K for this

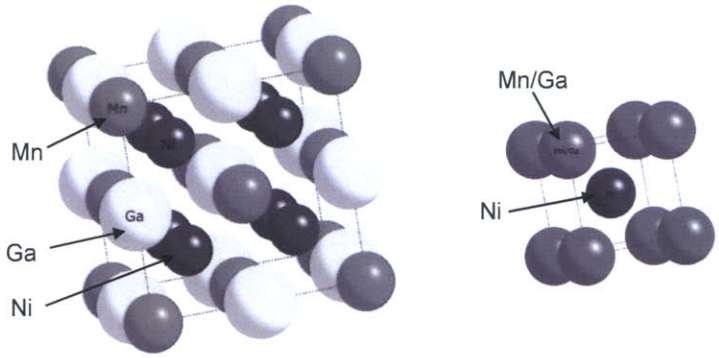

(a) (b)

Figure 2-1: (a) $L2_1$ (Heusler) structure of austenitic Ni_2MnGa. (b) B2 structure of high temperature phase, where Mn and Ga have become disordered. From Richard [31].

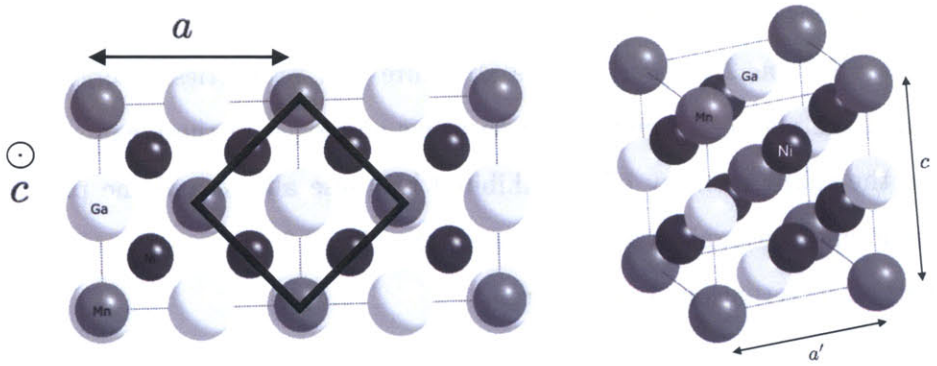

(a) (b)

Figure 2-2: (a) Relationship between new and original unit cells. (b) Face-centered tetragonal unit cell of martensitic Ni–Mn–Ga. From Richard [31].

composition [35], the lattice structure becomes tetragonal. Figure 2-2(a) shows a top view of two adjacent unit cells of the original austenite phase that have undergone the transformation to martensite. The dimensions, in the two crystallographic directions in the plane of the page, remain equal with lattice constant a . The third dimension, out of the plane of the page, contracts, and this new dimension is labeled c.

It should be noted that due to the new symmetry that develops, the structure is represented by a different unit cell. The relationship between the two is shown in Figure 2-2(a), where the black diamond shows the new crystallographic directions. These are at 45 deg to the original directions, and have dimension $a' = \frac{a}{\sqrt{2}}$. The new unit cell is shown in Figure

2-2(b), where it may be seen that $a' < c$. The structure is now face-centered tetragonal with $I4/mmm$ symmetry. For simplicity, however, the martensitic structure is often described in relation to the original austenite cell, by a body-centered tetragonal cell in which $c < a$. [31]

It is the difference between the lattice constants that determines the maximum shear strain that can be achieved through twinning of the martensite. The relation is given by

$$\epsilon_0 = 1 - \frac{c}{a}, \tag{2.1}$$

and

$$\gamma_0 = 2\epsilon_0, \tag{2.2}$$

where ϵ_{max} is the maximum shear strain and γ_0 is the maximum engineering shear strain. Throughout this thesis, unless otherwise indicated, the engineering shear strain is reported. Based on reported lattice constants for the stoichiometric composition, $a = 5.90$ Å, $c = 5.54$ Å [18, 35], we obtain $\gamma_0 = 12.20\%$ ($\epsilon_0 = 6.10\%$). The twinning mechanism is described in greater detail in Section 2.2.1.

2.1.2 Compositional Effects

By varying the composition from the exact stoichiometry of Ni_2MnGa, it is possible to effect significant changes in the thermal and mechanical properties of the alloy. Certain composition ranges have been found to have martensitic transformation temperatures above room temperature, which allows actuation without cooling [2, 25].

Changes in composition can also have an important effect on the structure of the low-temperature martensite phase. In particular, the martensite formed by the stoichiometric composition is a modulated, five-layered tetragonal structure, denoted 10M, where the modulation refers to a periodic, ordered, small displacement of atomic planes. For certain compositions with less than 50 at% Ni and more Mn than Ga, the martensite develops as a seven-layered, or 14M, martensite [31]. This structure is not tetragonal but orthorhombic, with three unique lattice constants $a \neq b \neq c$. The ratio of the shortest dimension to the longest, c/a, is smaller than in the tetragonal martensite, giving a maximum strain

of approximately $\gamma_{max} = 20\%$ ($\epsilon_{max} = 10\%$). Recently, there have been several reports of successful magnetic actuation of the orthorhombic phase ([32, 21]).

Impurities in the alloy also play a role in its properties. Inclusions or other lattice defects can act as stress concentration points that may lead to the nucleation of twin boundaries [1], but can also act as obstacles to twin boundary motion if their pinning strength exceeds the actuation stress [16, 31]. In prior work, sulfide and titanium-rich precipitates were found, thought to have originated from impurities in the manganese in the alloy. While the latter were very small in size and unlikely to obstruct twin boundary motion, the sulfide inclusions were as large as 1 μm and were thought to contribute to the low twin mobility of these samples. [31]

More recently, samples cut from one of the single crystal boules were found to exhibit multiple, incompatible twinning systems, and to crack easily during sample preparation and attempted actuation. Further analysis of the samples by backscattered electron (BSE) microscopy revealed the presence of tantalum inclusions. These inclusions, a product of the tantalum plates used to purify the manganese, were approximately 400–700 nm in size and tended to align in groups up to 100 μm in length. [31]

Figure 2-3(a) shows an array of these groups, cutting across the fracture surface of a single crystal that cracked during actuation. The inclusions appear as thin white scratch marks bisecting several of the twin boundaries, which extend roughly horizontally across the image. The image was taken using BSE microscopy, which causes heavier elements to appear brighter. Figure 2-3(b) shows a higher magnification image of one of these chains of inclusions, approximately 80 μm in length [30]. Again, the tantalum inclusions appear as bright spots at the center of the crack. Extensive plastic deformation is visible in the vicinity of the inclusions. It is likely that these inclusions contributed to the poor actuation behavior of the sample in question, acting as obstacles to twin boundary motion and aiding in the formation and propagation of cracks.

2.1.3 Properties of Single-crystalline Ni–Mn–Ga

Table 2.1 shows accepted values for some thermal, magnetic and mechanical properties of Ni–Mn–Ga single crystals in the tetragonal, martensitic phase [3]. Since many properties

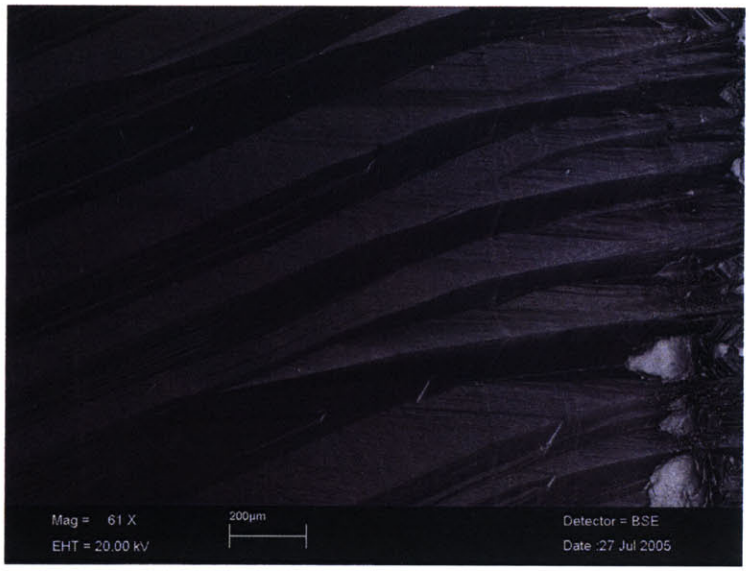

(a)

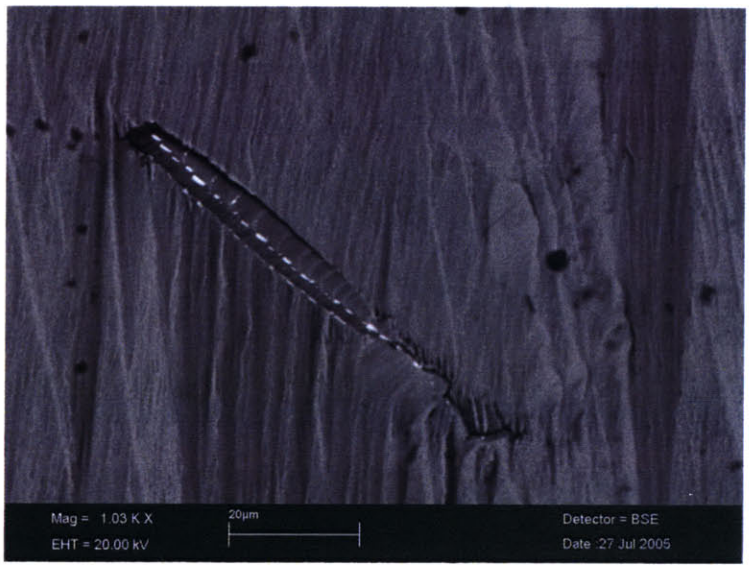

(b)

Figure 2-3: (a) Low magnification BSE image of a single crystal fracture surface. Step-like features are twins that have moved to the fracture surface. The thin, bright, nearly vertical marks cutting across the twins are chains of tantalum inclusions. (b) Higher magnification of a chain of tantalum inclusions, approximately 80 μm in length. Again, BSE reveals the heavier, tantalum-rich inclusions as the bright spots at the center of the crack. [30]

Property	Symbol	Value
Martensite start temperature	T_m^s	32 °C ± 30°C
Tetragonality	c/a	0.94
Twinning shear strain	$\epsilon_0\,(\gamma_0)$	0.062 (0.124)
Twin boundary angle (Relative to $\langle 100 \rangle$)	β	43 deg
Saturation magnetization	M_s	$4.8 \times 10^5\,\mathrm{Am}^{-1}$
Magnetocrystalline anisotropy energy	K_u	$1.9 \times 10^5\,\mathrm{Jm}^{-3}$
Threshold magnetic field for actuation	H_0	$1.2 \times 10^5 \pm 0.2 \times 10^5\,\mathrm{Am}^{-1}$*
Threshold twinning stress	τ_0	1.0 ± 0.5 MPa*
Mass density	ρ	$8.1 \times 10^3\,\mathrm{kg\ m}^{-3}$

Table 2.1: Accepted approximate values for properties of single-crystalline Ni–Mn–Ga in the tetragonal martensite phase. From [3]. (Values marked with an asterisk are typical of a well-conditioned single crystal of Ni–Mn–Ga. For example, improper thermomechanical treatment or insufficient conditioning can lead to twinning stresses as high as 10 MPa.)

are highly dependent upon composition and defect distribution, they can only be given approximately.

Single-crystalline, martensitic Ni–Mn–Ga has a tetragonal structure, so the elastic stiffness tensor has six independent components. Using Voigt notation for these components c_{ij}, the constitutive relation may be expressed as

$$\begin{pmatrix} \frac{1}{\sqrt{2}}(\sigma_{xx}+\sigma_{yy}) \\ \sigma_{zz} \\ \frac{1}{2}(\sigma_{xx}-\sigma_{yy}) \\ \tau_{xy} \\ \tau_{yz} \text{ or } \tau_{zx} \end{pmatrix} = \begin{pmatrix} c_{11}+c_{12} & \sqrt{2}c_{13} & & & \\ \sqrt{2}c_{13} & c_{33} & & & \\ & & c_{11}-c_{12} & & \\ & & & c_{66} & \\ & & & & c_{44} \end{pmatrix} \begin{pmatrix} \frac{1}{\sqrt{2}}(\epsilon_{xx}+\epsilon_{yy}) \\ \epsilon_{zz} \\ \frac{1}{2}(\epsilon_{xx}-\epsilon_{yy}) \\ 2\epsilon_{xy} \\ 2\epsilon_{yz} \text{ or } 2\epsilon_{zx} \end{pmatrix}, \tag{2.3}$$

when the x-, y- and z-axes are aligned with the crystallographic directions. From Equation 2.3, it may be seen that the constants $c_{11}+c_{12}$, c_{13} and c_{33} govern dilatational strain, while c_{66} and c_{44} control rhombohedral deformation. Tetragonal deformation is governed by the constant $c_{11}-c_{12}$. Dai *et al.* [6] have measured these elastic constants using a continuous

wave method and obtained the values

$$\begin{pmatrix} c_{11}+c_{12} & \sqrt{2}c_{13} & & & & \\ \sqrt{2}c_{13} & c_{33} & & & & \\ & & c_{11}-c_{12} & & & \\ & & & c_{66} & & \\ & & & & c_{44} & \end{pmatrix} = \begin{pmatrix} 69 & 39 & & & & \\ 39 & 28 & & & & \\ & & 9 & & & \\ & & & 49 & & \\ & & & & 51 & \end{pmatrix} \text{GPa.} \qquad (2.4)$$

It is immediately apparent from Equation 2.4 that the constant $c_{11} - c_{12}$ is much smaller than the others. This behavior is typical of a near second order shape memory alloy [6], and is associated with a shear on a $\{110\}$ plane in a $\langle 1\bar{1}0 \rangle$ direction. Due to the softness of the crystal in tetragonal deformation, shear waves polarized along these planes in $\langle 1\bar{1}0 \rangle$ directions are attenuated strongly. The resulting dissipation of energy can make accurate determinaton of the tetragonal stiffness constant very difficult, since the echoes from waves of this type are often too faint to be measured [33].

2.2 Shape Memory Effect in Ni–Mn–Ga

2.2.1 Twinning of Tetragonal Martensite

When subjected to a shear stress of sufficient magnitude, martensitic Ni Mn Ga is able to deform by twinning. This deformation mechanism is observed in certain metals and alloys with body-centered or face-centered lattice structures. For materials with body-centered structures, such as copper, the yield stress is usually lower than the threshold twinning stress, so slip is the dominant deformation mechanism. Conversely, for certain materials with face-centered lattice structures (e.g., Fe, Ni–Mn–Ga), twinning becomes the most important deformation mechanism at low temperatures [5]. In the martensitic Ni Mn–Ga alloys studied here, the twinning stress is in the range of 1.0 ± 0.5 MPa, several orders of magnitude below the plastic yield stress.

Twinning differs from plastic deformation in that it is fully reversible when all conditions are reversed, and is limited to a discrete displacement per atomic plane. The mechanism

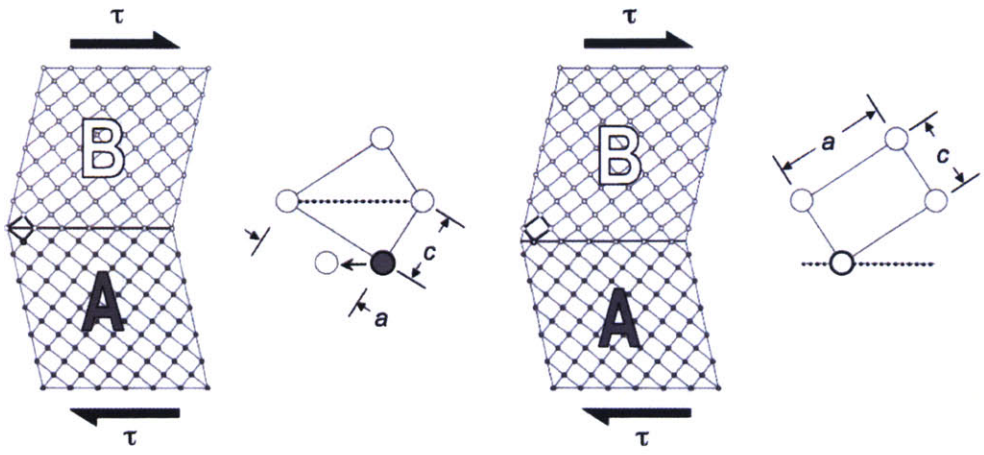

(a) (b)

Figure 2-4: Schematic illustration of the twinning of a tetragonal martensite. The figure shows the configuration of the crystal before (a) and after (b) motion of a twin boundary by a single atomic layer, resulting in the growth of the extent of variant B. Note that the difference between the lengths of the a- and c-axes has been exaggerated greatly to aid in visualization.

is illustrated in Figure 2-4. Here, a single crystal of Ni–Mn–Ga is shown, consisting of two martensitic variants A and B. In Figure 2-4(a), half of the crystal is in each variant. The interface between them, the twin boundary, forms a plane across which the crystal structure of each variant is the geometrical reflection of the other, giving rise to the term "twinning." When a shear stress $\tau > \tau_0$, where τ_0 is the twinning stress, is applied as shown, atoms of variant A immediately below the twin boundary are induced to move to variant B sites. A single unit cell undergoing this transformation is magnified to the right of each figure. When all of the atoms in the plane below the twin boundary move in this manner, the twin boundary moves down by one atomic layer, and the extent of variant B grows at the expense of variant A, and as shown in Figure 2-4(b). The longer crystallographic axis, labeled a in Figure 2-4(a), becomes a shorter c-axis in the transformation.

Recently, Müllner *et al.* have developed a microscopic model of twin boundary motion in Ni–Mn–Ga [20, 23]. According to the model, the process by which the twin boundary progresses from one atomic layer to the next is by the cooperative motion of twinning disconnections (also called twinning dislocations). When the shear stress on the twin boundary plane exceeds the twinning stress, a twinning disconnection forms a step on the twin bound-

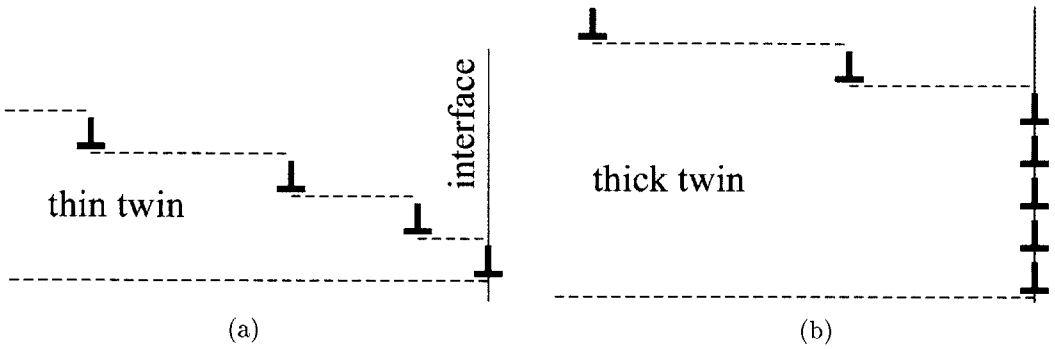

Figure 2-5: Schematic representations of a thick and a thin twin. (a) For the thin twin, t is small and so τ_c is large. The applied stress cannot overcome the repulsion between adjacent disconnections, preventing them from reaching the interface. (b) Due to the thickness of the twin (large t), τ_c is low enough that subsequent twinning disconnections are able to reach the interface, forming a disconnection wall. From [23].

ary. With continued application of stress, the disconnection is induced to move across the twin boundary. When it has traversed the entire width of the crystal, the twin boundary has moved one atomic layer; the twin achieves a stable configuration, and the deformation will remain after the stress is removed.

Müllner *et al.* [22, 23] also propose that the thickness of the twin (or martensitic variant) may have an important effect on the ability of the variant to grow in extent by twin boundary motion. According to this model, the critical shear stress τ_c to move a disconnection to an interface (e.g., a grain boundary in polycrystalline Ni–Mn–Ga, or a face of the single crystals studied here), is given by

$$\tau_c = \frac{Gd}{4\sqrt{2}(1-\nu)t}, \tag{2.5}$$

where G is the shear modulus, d is the spacing between disconnections in the direction normal to the twinning plane, ν is the Poisson ratio and t is the twin thickness. Schematic representations of a thick and a thin twin are shown in Figure 2-5. In Figure 2-5(a), a thin twin has formed by the motion of the bottom disconnection to the interface, forming the beginning of a disconnection wall (manifested as the visible edge of the twin boundary in a single crystal). Subsequent disconnections form steps in the twin boundary, but are repelled by one another and thus remain separated by a distance that is large compared to the interplanar spacing. Since τ_c is inversely proportional to the twin thickness t, the

critical stress is too large to allow further growth of the disconnection wall. For the thick twin shown in Figure 2-5(b), τ_c is sufficiently reduced that subsequent disconnections can move to the interface, growing the disconnection wall and hence the thickness of the twin. As illustrated in [23], disconnections on a thin twin with $t = 10\,\text{nm}$ would require on the order of $\tau_c = 10^{-2}\,G$ to move, which according to the value of G given in Equation 2.4 would be approximately 90 MPa. For a thick twin with $t = 100\,\mu\text{m}$, however, $\tau_c \simeq 10^{-6}\,G$, which is approximately 9 kPa. Disconnections on this twin could be moved easily, either magnetically or mechanically.

Since the total number of twinning disconnections in a twin, N, is given by

$$N = \frac{t}{d}, \tag{2.6}$$

an alternative expression of Equation 2.5 is

$$\tau_c = \frac{G}{4\sqrt{2}(1-\nu)N}. \tag{2.7}$$

Thus, the critical shear stress to move a twinning disconnection is inversely proportional to the total number of twinning disconnections.

Because lattice defects can act as twin boundary nucleation sites [1], it is likely that they can act as disconnection sources. This phenomenon is analogous to the manner in which the high stress fields associated with defects can act as dislocation sources in plastic deformation. Ahluwalia *et al.* [1] have simulated the effect of defect size on stress-induced martensite formation in FePd, and have found that the larger the defect, the earlier the transformation nucleation. It stands to reason, therefore, that a certain number of defects may be beneficial to actuation.

2.2.2 Impediments to actuation

In section 2.2.1, it was seen that lattice defects can act as twin boundary nucleation sites, and therefore aid in actuation. Depending upon the type and strength of the defect, however, it may hinder actuation instead. Again, an analogy to dislocation theory can be illustrative.

The force exerted upon a dislocation as it approaches a defect can be either attractive or repulsive. For example, an edge dislocation approaching a solute atom in the plane above the slip plane will have a positive interaction energy (repulsive force) if the atom is larger than the host atoms, and a negative interaction energy (attractive force) if it is smaller. Although locations of positive and negative interaction energy may be distributed evenly throughout the crystal, the dislocations will tend to "linger" around points where the force is attractive. The net effect of this behavior is that defects tend to obstruct dislocation motion, and hence increase the yield stress. [5]

Furthermore, it is noted that interstitial atoms in body-centered cubic metals tend to create tetragonal distortions of the lattice. These defects lead to large shear strains, and hence large shear stresses, in their vicinity. For this reason, tetragonal defects are much more substantial obstacles to dislocation glide than other types of defect [5]. If any of the impurities discussed in Section 2.1.2 consist of solute atoms sitting at interstitial sites in the Ni–Mn–Ga lattice, they could create such a tetragonal distortion and thus act as "hard" obstacles to dislocation glide.

The characteristic twinning stress of a crystal is directly dependent upon the strength and distribution of obstacles to twin boundary motion. These may be inclusions or other lattice defects, which present an energy barrier that must be overcome in order for the twin boundary to pass through. Crystals, similar in composition and twin boundary mobility to those studied here, were studied extensively by Marioni [15, 16]. It was found that the strength of the obstacles was broadly distributed, but that the largest number were in the vicinity of 1.1×10^5 J m^{-3}. The stress necessary to move twin boundaries past obstacles of this strength was approximately 1.7 MPa.

Another important obstacle to twin boundary motion, and hence effective actuation, is the presence of incompatible twinning systems. Twinning can only take place along certain crystallographic planes, which are $\{110\}_A$-type. The subscript A indicates that the plane normal is given with respect to the original, austenitic structure, following [31]. This convention is adopted due to the complexity of the crystallographic notation for the tetragonal structure. For the undeformed structure, there are six possible twin planes: $(110)_A$, $(1\bar{1}0)_A$, $(101)_A$, $(10\bar{1})_A$, $(011)_A$, and $(01\bar{1})_A$. The goal in preparing samples for actuation is to ob-

tain a single active twinning sytem. This result may be accomplished by the application of an appropriate stress, either magnetically or mechanically, during cooling from the high-temperature, austenite phase (see Chapter 3). If successful, this procedure creates a single variant state when the crystal enters the martensite phase. A second shear stress is then applied, in the desired actuation direction which, ideally, activates only the desired twinning stystem.

In practice, the activation of a single twinning system is difficult to achieve. For example, suppose one wishes to induce twinning across the $(110)_A$ plane. A pure shear stress on the $(110)_A$ plane in the $[\bar{1}10]$ direction will favor this system, but due to the conservation of angular momentum the $(1\bar{1}0)_A[\bar{1}\bar{1}0]$ twinning system is favored equally. Due to the aspect ratio of the crystals used here, one of these twin plane orientations is geometrically less favorable, and the activation of that system is seldom observed. Of greater concern are the twinning systems with planes that lie at oblique angles to the desired plane, in this case the $(101)_A$, $(10\bar{1})_A$, $(011)_A$, and $(01\bar{1})_A$ planes. Due to their orientation, these planes experience a resultant shear stress along them which, while less than the component on the desired plane, may lead to twinning if other factors (e.g., defect distribution, thermomechanical history) contribute to lower their effective energy with respect to the desired system.

When two incompatible twinning systems intersect, they tend to "lock up." Effectively, this produces an interface, at which disconnection walls can form. Disconnection walls are associated with strong stress fields normal to the plane of the wall, which are compressive on one side of the wall and tensile on the other, and therefore tend to form crack nucleation sites [23]. Müllner *et al.* [23] explain that, as long as all aspects of disconnection motion are reversible, these cracks can open and close during cyclic actuation while maintaining a stable length and not propagating further. When some detail of the motion becomes irreversible, however, for example due to plastic deformation, the crack can grow and fracture can occur. Figure 2-6 shows an example of a fracture surface thus formed. In Figure 2-6(a), the surface is seen to be highly faceted, evidence of motion along multiple twinning planes lying at oblique angles to each other. In Figure 2-6(b), a higher magnification image gives a clearer picture of one of these facet surfaces, with certain features that likely indicate an additional, ductile mode of failure.

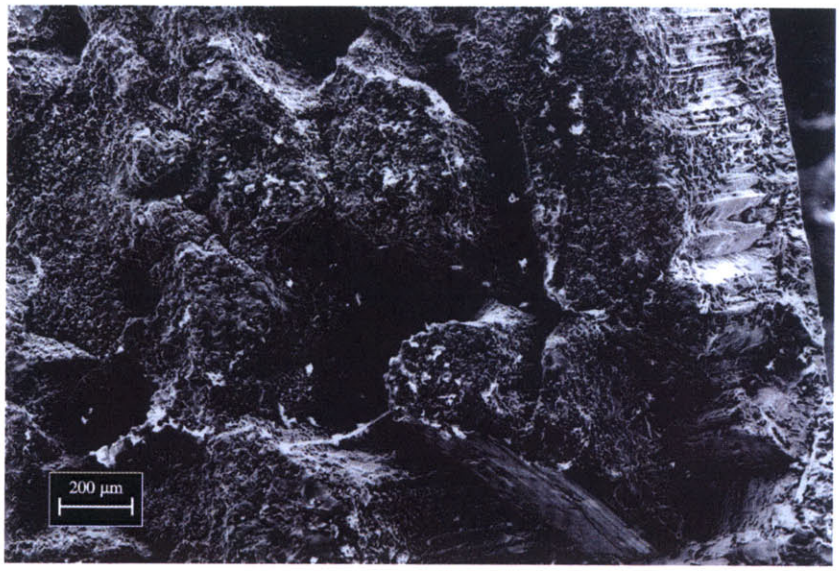

(a)

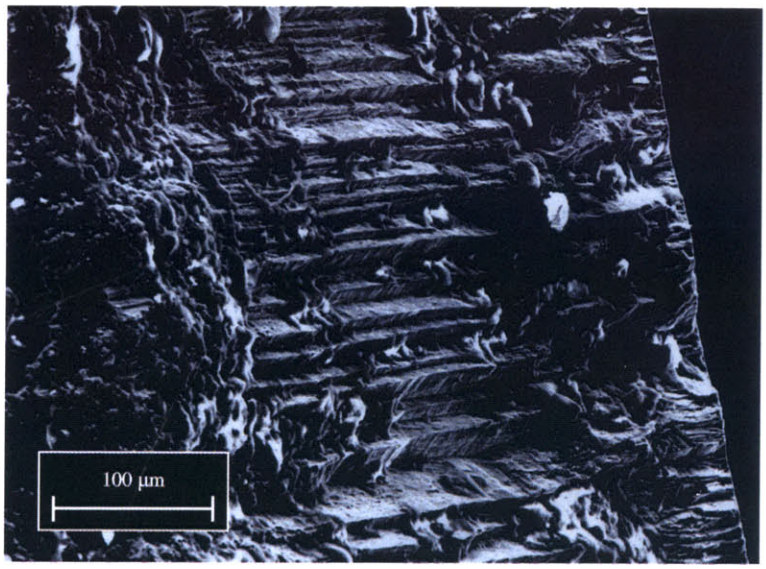

(b)

Figure 2-6: Fracture surfaces due to the intersection of incompatible twinning systems. (a) Low magnification image SEM image of fracture surface. Extensive faceting reveals the presence of multiple twinning systems. (b) Higher magnification image of fracture surface, showing twins that have moved to the interface. The tangled features most likely result from an additional, plastic mode of failure.

2.3 Acoustic Actuation

As discussed, the shear stress necessary to initiate twin boundary motion may be generated either magnetically or mechanically. The focus of this thesis is on the actuation of Ni–Mn–Ga crystals by a third method, the propagation of asymmetric acoustic stress pulses. In order to understand the underlying mechanism, it is instructive to review some elementary aspects of wave theory.

2.3.1 Linear Elastic Wave Theory

The simplest form of wave motion in an elastic medium is the propagation of longitudinal waves in a slender rod. If $l \ll d$, where l is the length of the rod and d its diameter, so that the effects of longitudinal inertia may be neglected, and a simple one-dimensional approximation may be made. The governing equation for wave motion is

$$\frac{\partial^2 u}{\partial x^2} = \frac{1}{c_L}\frac{\partial^2 u}{\partial t^2}, \tag{2.8}$$

where u is the displacement, x is the spatial coordinate and t is time. The longitudinal wave speed c_L is related to the Young's modulus E, and the density ρ, by

$$c_L = \sqrt{\frac{E}{\rho}}. \tag{2.9}$$

For this type of wave, the wave speed c_L is the constant of proportionality relating the frequency of a wave, f, to its wavelength, λ, by the relation

$$c_L = f\lambda. \tag{2.10}$$

The solution to Equation 2.8 has the form

$$u(x,t) = f(x - c_L t) + g(x + c_L t), \tag{2.11}$$

where f and g represent right- and left-going waves, respectively. If only the right-going

wave is considered, for simplicity, the material velocity at point x and time t will be given by

$$v(x,t) = \frac{\partial u}{\partial t} = -c_L f'(x - c_L t). \tag{2.12}$$

The longitudinal stress, σ, is related to the strain $\epsilon = u_{x,x}$, by

$$\sigma(x,t) = E\frac{\partial u}{\partial x} = Ef'(x - c_L t). \tag{2.13}$$

From Equations 2.12 and 2.13, we obtain

$$\sigma(x,t) = -\frac{E}{c_L} v(x,t). \tag{2.14}$$

As seen in Equation 2.14, the stress at point (x,t) is directly proportional to the material velocity at that point. This result is general and applicable to the situation under investigation here, provided the material remains below its yield strength. This assumption is implicit in the small-strain approximation of linear elastic wave theory. Another property that is most easily understood in this one-dimensional approximation is the scattering behavior of an incident wave at an interface, where a reflected wave with a fraction R of the incident amplitude will be reflected, and a fraction T will be transmitted. If we consider the scattering at an interface between two rods of different cross-sectional area $A_1 \neq A_2$, $\rho_1 \neq \rho_2$, and/or $E_1 \neq E_2$, the values of these coefficients will depend on the relative impedances Z_1 and Z_2 of the rods, where

$$Z = A\sqrt{E\rho}, \tag{2.15}$$

according to the relation

$$R = \frac{Z_2/Z_1 - 1}{1 + Z_2/Z_1}, \quad \text{and} \quad T = \frac{2(Z_2/Z_1)(A_1/A_2)}{1 + Z/Z_1}, \tag{2.16}$$

as derived in Graff [8]. Equations 2.16 do not apply for more complicated waves such as dispersive, flexural waves. However the dependence of the sign of the coefficient on the relative impedances can be generalized. Specifically, it can be noted that when $Z_2 < Z_1$, $R < 0$. The implication is that an incident wave arriving at a traction-free surface, such

as the free end of a rod, the reflected wave is of opposite sign to the incident wave. Thus, the sign of the stress is reversed as the wave is reflected. In order for the reflected waves to induce a stress of the same sign as the incident waves, the second medium must have a higher impedance than the first. As expected, for the case where the rods are identical, there is no effective interface; $Z_1 = Z_2$ and $R = 0$.

Because the mode of actuation studied here is by the propagation of bulk shear, rather than longitudinal wave pulses, there are certain features of the linear approximation for transverse waves in a narrow beam that are worth noting. This approximation neglects the effects of rotatory inertia, and is based upon Bernoulli-Euler beam theory, i.e., it assumes that plane cross-sections remain plane, and normal to the neutral axis, as the beam is deflected. The further assumption is made that the beam is not loaded, and that the cross-section and material properties do not vary with length. With these restrictions in mind, the governing equation for wave motion is

$$\frac{\partial^4 y}{\partial x^4} = -\frac{\rho A}{EI}\frac{\partial^2 y}{\partial t^2}, \tag{2.17}$$

where y is the spatial coordinate perpendicular to the direction of wave propagation, which is the x-direction. A is the cross-sectional area of the beam and I its moment of inertia. The most important feature to note from Equation 2.17 is that, since the beam bending equation $M = EI\kappa$ relates the moment, M, to the curvature, $\kappa = \frac{\partial^2 y}{\partial x^2}$, the wave equation contains a fourth-order partial derivative in x. This load-deflection relation results in a non-linear relationship between frequency and wavelength. In other words, there is no relation analogous to Equation **??**, and the coefficent of the time derivative in Equation 2.17 does not have units of velocity. The result is that different frequency components of the acoustic signal will travel at speeds. This phenomenon, known as dispersion, results in the "spreading" of an incident pulse over time. A corollary of this phenomenon is that there exists a critical frequency ω_c below which waves do not propagate into the material; vibrations at the surface are evanescent, in that they are rapidly attenuated to zero after traveling a short distance.

Because the above approximation assumes that the length of the beam is much greater than its width, it cannot describe fully the behavior of crystals of the shape under investi-

gation. A third scenario examines the propagation of elastic waves in an infinite half-space. This approach does not admit the side boundaries of the crystal, assuming that the material extends infinitely in all directions except one, which forms the surface of the half-space.

The governing equations will not be derived here but, from [19], may be expressed as

$$\frac{\partial^2 \phi}{\partial x^2} + \frac{\partial^2 \phi}{\partial y^2} = \frac{1}{c_L} \frac{\partial^2 \phi}{\partial t^2}, \tag{2.18}$$

$$\frac{\partial^2 H_p}{\partial x^2} + \frac{\partial^2 H_p}{\partial y^2} = \frac{1}{c_T} \frac{\partial^2 H_p}{\partial t^2}, \; p = x, y, z, \tag{2.19}$$

where the scalar ϕ and vector $\mathbf{H}$ are the displacement potentials associated with dilatational and shear deformation, respectively, and c_T is the speed of propagation of the shear wave. For an isotropic solid, the two wave speeds c_L and c_T are related by

$$\frac{c_L}{c_T} = \sqrt{\frac{2 - 2\nu}{1 - 2\nu}}. \tag{2.20}$$

As may be seen from Equation 2.20, the shear wave moves at a lower velocity than the dilatational wave. In fact, it is a general result that a wave associated with a deformation of modulus M propagates at a speed c_M given by

$$c_M = \sqrt{\frac{M}{\rho}}. \tag{2.21}$$

For example, for shear waves oriented along the twinning plane in Ni–Mn–Ga, the relevant constant is $M = c_{11} - c_{12}$, the modulus for tetragonal deformation (see Section 2.2.1). This gives a wave speed c_{tetra} of

$$c_{\text{tetra}} = \sqrt{\frac{c_{11} - c_{12}}{\rho}}. \tag{2.22}$$

Substituting the relevant modulus from Equation 2.4, and the density from Table 2.1, we obtain an estimated wave speed of $c_{\text{tetra}} = 1050\,\text{ms}^{-1}$, much lower than the longitudinal wave speed of the material.

The simple theory outlined above is of limited utility in explaining quantitatively the results of these experiments, for several reasons. First, the theory is valid only for small dis-

placements, and it does not take into account plasticity or any nonlinear material properties. It assumes a linearly elastic, isotropic solid, which is clearly not the case for a single crystal of Ni–Mn–Ga. Finally, the geometry and types of waves generated in the experiments are not amenable to approximation by either longitudinal waves in a rod or transverse waves in a beam. In addition, the irregularly-shaped pulses generated here cannot be treated as harmonic wave-trains; a full analysis of the propagation and scattering behavior of these pulses would require all frequency components to be considered, by taking the Fourier transform of the pulse shape. Nevertheless, it can be illustrative to examine certain common or analogous properties of linear elastic waves, to gain a better qualitative understanding of the principles behind acoustic actuation.

2.3.2 Actuation by the Propagation of Asymmetric Stress Pulses

If a sinusoidal, harmonic wave is propagated into the Ni–Mn–Ga crystal in the absence of any external load, the stress experienced at a particular point in the crystal will oscillate between positive and negative values. Thus, any impetus given to atoms in the crystal to move in one direction is exactly reversed in the second half of the cycle. In order to effect uni-directional strain leading to twin boundary motion, then, it is necessary to generate a wave in which the maximum stress in one direction exceeds the twinning stress, while the maximum stress of the opposing sign does not. This result could be achieved by the imposition of either a static magnetic field or a static mechanical load, which would bias the crystal in one direction, or by propagating asymmetric stress pulses. It is the latter approach that is investigated here.

From Equation 2.14, it is known that the stress induced at a particular point in the material will be proportional to the material velocity at that point. Thus, by generating a highly asymmetric, sawtooth-shaped pulse with $t_r \ll t_f$, where t_r is the rise-time and t_f the fall-time of the pulse, it is possible to induce a large stress during the rise of the pulse, and a much smaller stress during the fall. If the maximum stress exceeds the twinning stress, twin boundary motion may be initiated. [3, 4]

Once the twinning stress is exceeded, the wave likely dissociates into elastic and plastic components. This behavior is observed in materials that deform plastically. The elastic wave moves at a speed c_e, while the plastic wave moves at a slower speed c_p. The elastic wave

carries a stress equal to the yield (or, in this case, twinning) stress, while the plastic wave has an amplitude equal to the total stress. Because during plastic flow the modulus of the material will change as a function of the applied stress, the plastic wave is inherently dispersive. Thus, it will tend to spread and decrease in amplitude as it propagates. In addition, the energy necessary to cause plastic deformation may be dissipated by various damping mechanisms, causing a further decrease in the amplitude of the plastic wave. Eventually, the amplitude of the stress wave falls below the yield stress, and the remaining energy is propagated as an elastic wave. [14]

The plastic wave speed is the upper bound for dislocation velocity. For many materials, once the yield strength has been exceeded, dislocation velocity has been found to be a monotonically increasing function of the applied shear stress. For strain rates below a certain limit, many metals exhibit a linear relationship, i.e.,

$$F = Bv, \tag{2.23}$$

where F is the force acting on a unit dislocation length, v is the dislocation velocity and B is the drag coefficent. [13]

As will be seen in Chapter 4, there is evidence that a similar viscous damping mechanism exists for twin boundary motion. By measuring the average displacement at the tip of the crystal per pulse, u_p, as a function an applied assisting prestress τ_{pre}, it is possible to obtain a rough estimate of the viscous drag coefficient governing this rate-dependence. Here, the stress from the acoustic pulses remains constant, while the prestress acts to increase the total shear stress on the twinning planes. Because the prestress is below the twinning stress τ_0, twin boundary motion does not take place until the acoustic pulses begin. In order to calculate the velocity of twin boundary motion, it is necessary to know the time during which twin boundary motion takes place, which due to inertia may not be simply the time during which the pulse exceeds the twinning stress. If t_p is the time per pulse during which twin boundary motion takes place, the average velocity of the tip of the crystal during this time, v_c, will be given by

$$v_c = \frac{u_p}{t_p}. \tag{2.24}$$

The strain rate $\dot{\gamma}$ may then be expressed as

$$\dot{\gamma} = \frac{v_c}{l_c} = \frac{u_p}{t_p l_c}, \tag{2.25}$$

where l_c is the length of the crystal.

Finally, the drag coefficient B, which relates the stress to the rate of strain, may be expressed as

$$B = \frac{\tau}{\dot{\gamma}} = t_p l_c \left(\frac{\tau}{u_p} \right), \tag{2.26}$$

where τ is the applied stress, and B has units of $\mathrm{Ns/m^2}$. As will be seen in Chapter 4, the term in parentheses in Equation 2.26 may be estimated by the slope of a plot of u_p vs. the magnitude of an applied, static prestress.

Chapter 3

Experimental Procedure

This chapter describes the experimental apparatus and procedure used in these investigations. In Section 3.1, the preparation of the Ni–Mn–Ga single crystal samples is described. Section 3.2 details the transducers and circuitry employed to create the asymmetric stress pulses. Finally, Section 3.3 describes the experimental configurations and procedure.

3.1 Sample Preparation

3.1.1 Origin and Properties of Single Crystal Boule

The single crystal boule from which the smaller actuation samples were cut was grown by Tom Lograsso at the Ames Laboratory, using a Bridgman technique [29]. Purified nickel and gallium were used for the alloy. Since purified manganese is not available commercially, it was purified prior to alloying. The tantalum inclusions found in earlier samples and described in Section 2.1.2 were the result of contamination during this process. The elements were melted and drop cast together, and the resulting ingot was heated to 1350 °C for 1 h. The single crystal was then grown by withdrawing the crucible from the furnace at a rate of 5.0 mm/h. After cooling, the crystallographic directions were identified by Laue diffraction, and two cuts were made along $\{100\}_A$ surfaces to allow future determination of the orientation. The final boule had a nominal composition of $Ni_{52.4}Mn_{25.8}Ga_{21.8}$ (at%), with a slight compositional gradient along its length.

3.1.2 Cutting and Polishing of Samples for Transverse Actuation

Upon receipt of the boule, it was oriented using these surfaces and mounted on an aluminum plate. For the mode of actuation discussed here, the crystal was mounted such that the vertical axis was a $\langle 110 \rangle_A$ direction, and the edges of the plate were parallel to the $\langle \bar{1}10 \rangle_A$ and $\langle 001 \rangle_A$ directions. This plate was then mounted in a wire electric discharge milling (EDM) machine, with its edges squared to the machine axes. The boule was then cut with the vertical wire to give an elongated rectangular prism with a $\langle 110 \rangle_A$ long axis, and side faces which lie along $\{\bar{1}10\}_A$ and $\{001\}_A$ planes. The rounded ends, where the section intersected the boule surface, were cut by EDM along the $\{110\}_A$ planes, to give the final crystal shape.

During subsequent handling of the actuation sample, care was taken to avoid exerting large stresses on the crystal. If any such stress results in a shear stress along a potential twinning plane, of sufficient magnitude, it is possible to nucleate twin boundaries with undesired orientations. If nucleation occurs, it has been found that these incompatible twinning systems can persist even after annealing and extensive magnetic or mechanical conditioning. This precaution was particularly important during mechanical polishing of the samples. The samples were polished to a near mirror finish, both to aid in visualization of twin boundaries, and because surface asperities can act as stress concentration and thus crack nucleation sites. Also, a rough surface would introduce additional reflections of the stress waves from large asperities, which could reduce the effectiveness of the incident stress pulses. Because mechanical polishing produces large shear stresses, including on a $\{\bar{1}10\}_A$ face, and also requires a significant clamping force to keep the crystal in its holder, this process was the one most likely to nucleate undesired twins. In order to avoid twinning, the clamping and frictional forces must be no larger than necessary to achieve the desired surface quality.

3.1.3 Heat Treatment

After polishing, the samples were heat treated. This process reduces the presence of any plastic dislocations, as well as to help eliminate any existing twinning systems. As mentioned in Section 3.1.2, if the crystal is heavily twinned, or if any incompatible twins have intersected and locked, this treatment is not always successful at erasing the crystal's memory of these

twins.

The samples were wrapped in molybdenum wire and placed in quartz ampoules, along with a tantalum getter. The ampoules were then backfilled with argon, and sealed. The argon provides an inert atmosphere during heat treatment, and the getter reacts preferentially with any oxygen remaining in the tube. The molybdenum wire, which itself cannot react with the Ni–Mn–Ga, was used to prevent the crystal from coming into contact with the surface of the ampoule. If contact between the sample and tube were to occur, it could allow the diffusion of silicon into the crystal matrix, forming silicate inclusions.

The ampoules were then placed in a furnace. The temperature was increased, at a rate of 5 °C/min, to the maximum annealing temperature of 900 °C. This temperature was maintained for 24 h, and then lowered at a rate of 5 °C/min to 500 °C, which was held constant for 2 h. Above this temperature, the Mn and Ga atoms are disordered; at 500 °C the crystallographic structure acquires $L2_1$ (Heusler) ordering, as described in Section 2.1. Finally, the temperature was reduced at the same rate to 200 °C, which was held constant until the sample was removed from the furnace. The purpose of this final step was to keep the crystal in the austenite phase, preventing the formation of randomly oriented martensitic variants.

3.1.4 Magnetic Training

For the {100}-cut crystals used in prior work, for example by Chambers [3] (see Chapter 1), the crystal was biased in favor of a single twinning system by the application of a normal, compressive stress along the crystal's long axis during cooling to martensite. This state of stress has a maximum shear component along the twinning planes, which transect the crystal's length at about 45 deg in this mode of actuation. For the transverse mode of actuation described in this thesis, biasing the crystal mechanically would require the application of a shear stress directly to the ends of the crystal. Despite several efforts to apply a shear stress during cooling, it proved to be extremely difficult to accomplish with a crystal that was cooling rapidly from 200 °C, and would also tend to induce large bending moments in the sample. These complications led to the development of a purely magnetic conditioning method.

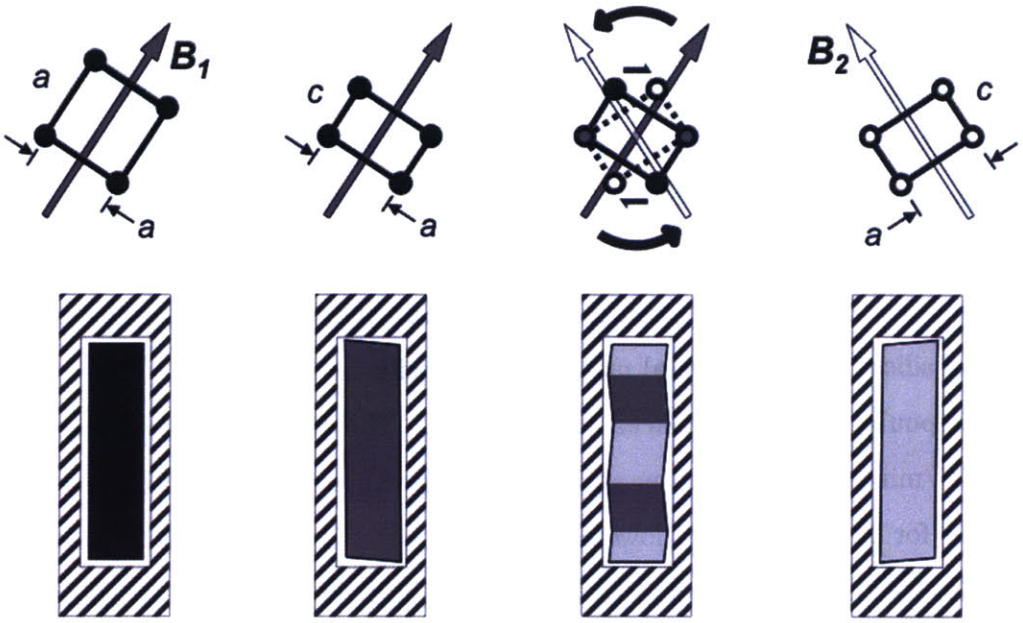

Figure 3-1: A {110}-cut crystal undergoing magnetic training during cooling. (a) High temperature, austenite phase; (b) martensite, variant A; (c) transformation to variant B; (d) variant B.

The samples were removed from the furnace and placed in a small toaster oven, to keep them at approximately 200 °C. The ampoule was broken and the molybdenum wire was unwrapped. Then, the sample was returned immediately to the oven. A rectangular aluminum holder, sized to surround the sample completely, and keep the sample oriented at 45 deg to the sides of the holder, was also placed in the oven. When both the holder and sample had reattained the maximum temperature, the sample was removed from the oven using tweezers and placed inside the holder.

The holder was placed between the poles of a large electromagnet, and a magnetic field of approximately 6 kG was applied. Due to the shape of the holder, the sample was held at approximately 45 deg to the field, which was therefore aligned with a crystallographic direction. Figure 3-1 shows the transformations taking place during the magnetic training process, from the frame of reference of the crystal (in fact, the crystal, not the field was rotated). In Figure 3-1(a), the crystal is still at approximately 200 °C, and the alloy is in

the cubic, austenite phase. Because all three lattice constants are equal, the crystal shows no tendency to align itself with the field. As the transformation to martensite takes place, however, the transformation to the shorter c-axis will tend to occur in the magnetization direction. Thus, upon cooling to room temperature in a strong magnetic field, the sample should be in a single martensitic variant state, with the c-axis aligned with the magnetic field (Figure 3-1(b)).

Figure 3-1(c) shows the key step for correct twin boundary nucleation. Here, the holder is rotated such that the field is aligned with what will become the c-axis direction of the second actuation variant. In order to avoid nucleating a variant that is incompatible with the mode of actuation, the field must be kept in the plane of the page. While tests have shown that it is possible to minimize the appearance of these incompatible twins during training, it is on the oblique planes (which are not parallel to any face of the crystal) that undesired twins are most likely to nucleate. Twin boundaries are unlikely to form parallel to the large face of the crystal because of the crystal's geometry. Such twins would have a very large surface area, and would therefore require a larger amount of energy to nucleate. However, twin boundaries oblique to the desired $\{110\}$ twin boundary may form, because the induced shear stress will have some component tangent to the oblique twinning plane, and the area of this plane is only slightly larger than that of the perpendicular cross-section. Similarly, once these twins have been nucleated, any stress applied to actuate the crystal in the desired direction will also have a component which, resolved normal to these planes, will tend to induce motion of these twin boundaries until they become pinned. Actuation of a sample with incompatible twinning systems will therefore tend to grow, and then lock in any undesirable martensitic variant.

Assuming one does obtain the correct two variants, there are two potential orientations of twin boundary between these variants: one perpendicular to the long axis of the crystal, which is the desired twinning system, and the other parallel to it. In other words, the goal is ensure that the twin boundaries are parallel to the small, end-faces rather than the large, $\{\bar{1}10\}_A$ face. As discussed in Section 2.2.1, the crystal's aspect ratio helps gives it a geometrical bias in favor of the correct twin boundary orientation. In order to reinforce this tendency, it is not just the final orientation of the magnetic field, but the direction in which

it is rotated, that is important.

A single crystal of Ni–Mn–Ga that is free to rotate will tend to align itself such that the c-axis lines up with the magnetic field direction. If, however, the crystal is constrained as shown, there will be a torque exerted by the crystal against the walls of the holder. The resulting equal and opposite torque exerted on the crystal by the holder can be resolved as a shear stress along the two potential twinning planes. In order to nucleate twin boundaries of the correct orientation, this stress must be oriented such that it tends to move atoms from sites of variant A to sites corresponding to variant B. As shown, in this case a counter-clockwise rotation of the field produces the correctly-oriented shear. If the field were rotated to the same final orientation in a clockwise direction, it would tend to nucleate variant B by shearing the two stationary atoms on the left and right of the unit cell in Figure 3-1(c), in a vertical direction with respect to each other. This rotation would therefore tend to favor the nucleation of twin boundaries that would be oriented vertically in the figure.

Once the crystal was in the second single-variant state, as shown in Figure 3-1(d), it was rotated clockwise to the position shown in Figure 3-1(a), then repeatedly rotated between the two orientations. This final step has the effect of improving twin boundary mobility as existing twins thicken and new ones are nucleated.

3.2 Asymmetric Stress Pulse Generation

3.2.1 Piezoelectric Stack Transducers

The acoustic stress pulses used for actuation in these experiments were produced by piezoelectric stack transducers. Piezoelectric stacks consist of multiple layers of piezoceramic, bonded together and connected in parallel electrically. This construction allows them to produce much larger displacements than single layer transducers.

In the first configuration, the shear waves were produced indirectly, by the propagation of longitudinal waves in a $\langle 100 \rangle$ direction (see Section 3.3.1 for a complete description of this configuration). To produce the longitudinal stress pulses, 33-mode piezoelectric stacks were used. Here, the first digit in the numerical prefix indicates the direction of the polarization

and applied electric field, and the second the resulting strain, using Voigt notation for both. In other words, if $\hat{\mathbf{i}}$, $\hat{\mathbf{j}}$ and $\hat{\mathbf{k}}$ are the unit vectors in the x-, y- and z-directions, respectively, a 33-mode actuator converts an electric field $E\hat{\mathbf{k}}$ into a longitudinal strain ϵ_{zz}. The longitudinal stacks were manufactured by Piezo Systems, Inc., model number TS18-H5-104, with dimensions 18.0 mm × 5.1 mm × 5.8 mm. These stacks have a rated voltage range of 0 V–100 V and cannot tolerate a reverse voltage. They have a capacitance of 1600 nF, a free deflection of 14.5 μm, and can exert a blocked force of 840 N. [34]

The second configuration (see Section 3.3.2) utilized a 15-mode piezoelectric stack to generate the shear waves directly. In this case, the prefix indicates that an applied field in the direction of polarization, $E\hat{\mathbf{i}}$ results in a shear strain γ_{xy}. The model used was a PICA$^{\text{TM}}$-Shear Piezo Actuator P-141.10, manufactured by Physik Instrumente. The stack has a cross-section of 10.0 mm × 10.0 mm, and is 12.0 mm tall. It is bipolar, with an operating voltage range of −250 V to +250 V. The 15-mode stack has a much lower capacitance than the 33-mode devices, only around 30 nF. It has a free displacement of 10 μm, and a can exert a maximum blocked force of 200 N. [12]

3.2.2 Pulse Generator Circuit

In order to drive the piezoelectric stacks, a custom pulse generator circuit was developed that could drive both the unipolar, 33-mode stacks and the bipolar, 15-mode stacks. Figure 3-2 shows a schematic of this circuit, which operates as follows. The fast side of the large asymmetric pulse is initiated by a smaller rectangular pulse from a pulse generator at $J1$. A transformer, $T1$, is used for impedance matching and isolation from the high-voltage circuit. Capacitors $C1$ and $C2$ are charged by the DC power supplies at $J6$, $J7$ and $J13$, $J14$. When the gate voltage of the Darlington transistor $Q1$ is reached, current is free to flow from the capacitors to the piezoelectric stack.

In dual stack mode, where the 33-stacks are used, the stacks are connected between $J11$, which is at 0 V, and either $J10$ or $J12$, which go from 0 V to +100 V. In this configuration, the relay at $J5$ switches the active terminal between $J10$ and $J12$, allowing two stacks to be controlled alternately. In single stack mode, where the 15-mode stack is used, the stack is connected between $J8$ and $J9$. In this case, the power supply at $J6$, $J7$ is floated to +250 V.

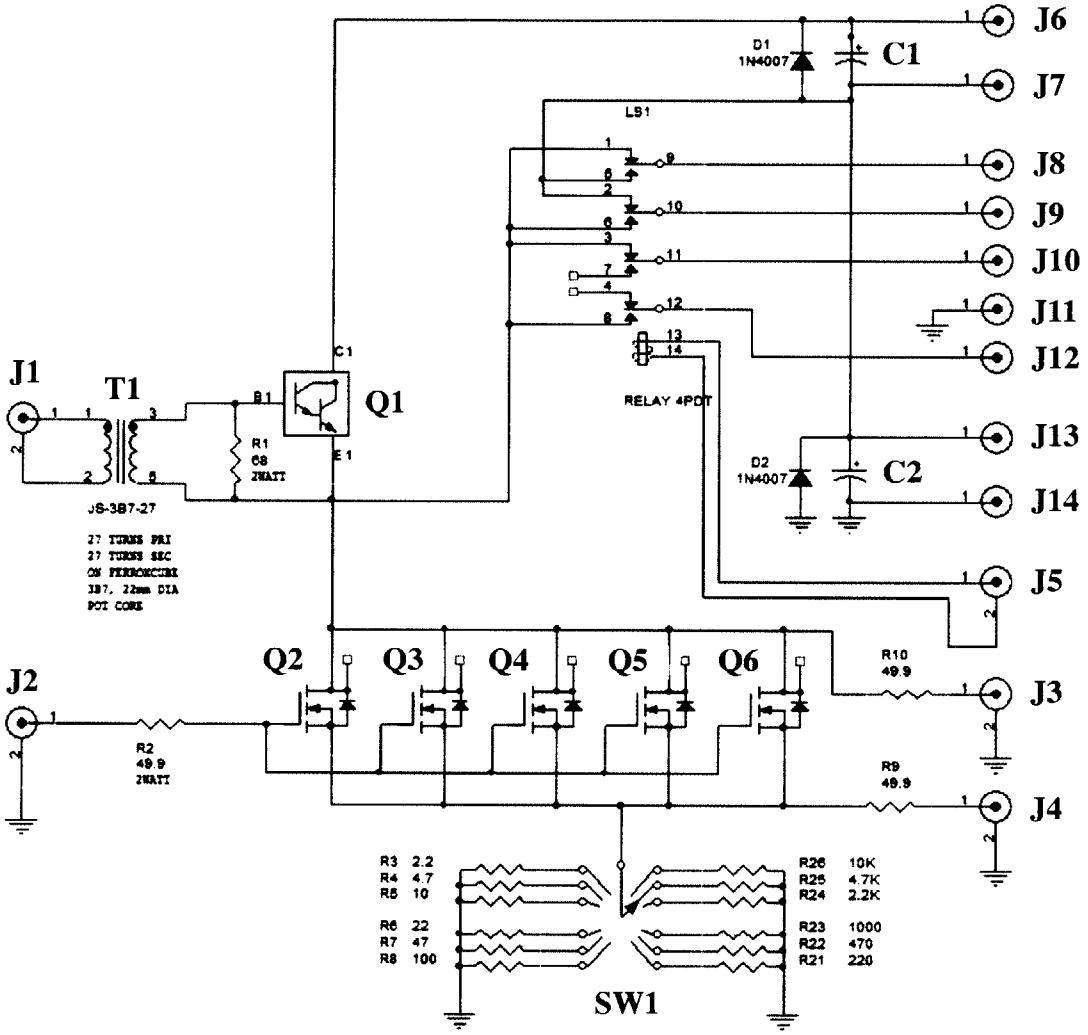

Figure 3-2: Schematic of the pulse generator circuit used to drive the piezoelectric stack actuators.

When the relay is in the position shown, terminal $J9$ remains at -250 V, while $J8$ rises rapidly from 0 V to $+500$ V when $Q1$ is switched. Relative to $J9$, then, $J8$ is pulsed from -250 V to $+250$ V. In this configuration, the relay switches the connections of $J8$ and $J9$, such that relative to $J9$, $J8$ pulses from $+250$ V to -250 V.

The triggering pulse is timed to last the duration of the stack charging time. When it is fully charged, a slow discharge is initiated by means of rectangular discharge pulse from the function generator at $J2$, which then switches the FETs $Q2 - Q6$. By adjusting the waveform voltage, and the resistance to ground using the switch $SW2$, it is possible to produce a constant drain current that discharges the stack completely, no faster than required to allow a given pulse repetition rate.

3.2.3 Typical Pulse Profile

If nonlinear, dynamic effects associated with rapid stack motion are neglected, the voltage on the stack may be assumed to be directly proportional to the stack displacement. Using the estimated total displacement of the stack, inferred from the motion of the tip of the FSMA when no twin boundary motion is taking place, the displacement profile of the stack can then be approximated using the voltage waveform. Due to the inertia of the attached apparatus and the rapid rate of motion, this displacement is in general less than the free displacement given in Section 3.2.1.

If the displacement of the stack is known, the stress can be estimated based on Equation 2.14. In this case, the modulus used is not E but the tetragonal deformation modulus given in Equation 2.4, $c_{11} - c_{12} = 9\,\text{GPa}$. By assuming that the stack velocity is equal to the material velocity in the FSMA at the interface, and given an estimated total displacement of $7.5\,\mu\text{m}$ for the 15-mode stack, the stress profile may be approximated by a constant multiple of the numerical derivative of the voltage profile. Figure 3-3 shows a typical such estimate for the 15-mode stack, with the maximum displacement of $7.5\,\mu\text{m}$ corresponding to $+250\,\text{V}$, and zero displacement corresponding to a stack voltage of $-250\,\text{V}$. As may be seen, the estimated maximum stress is approximately 4.5 MPa, which is greater than but of the same magnitude as the twinning stress. As will be seen in Chapter 4, there is evidence that the maximum stress is indeed of this order. Implicit in this estimate is the assumption that

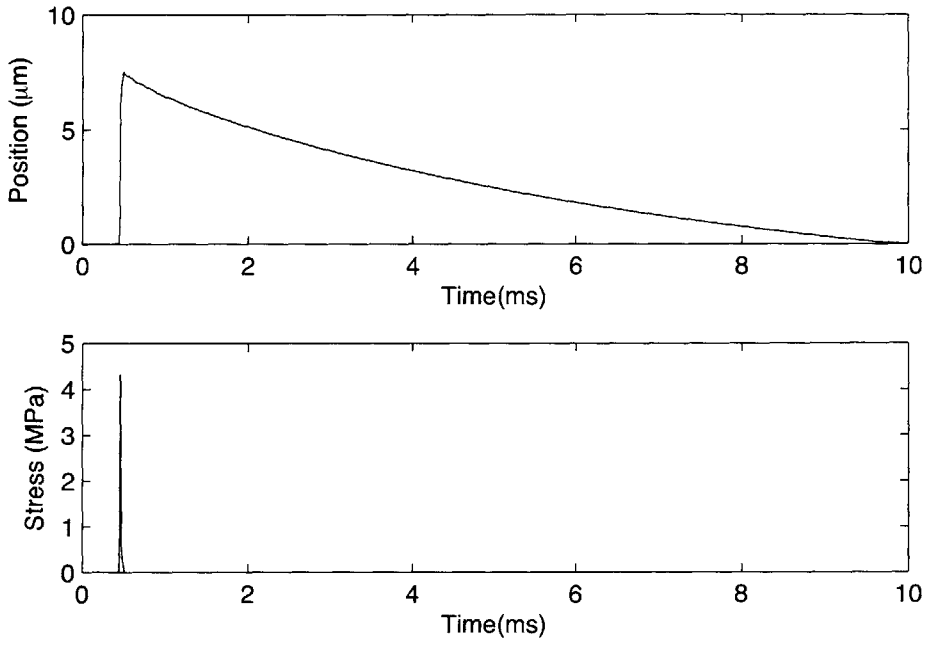

(a)

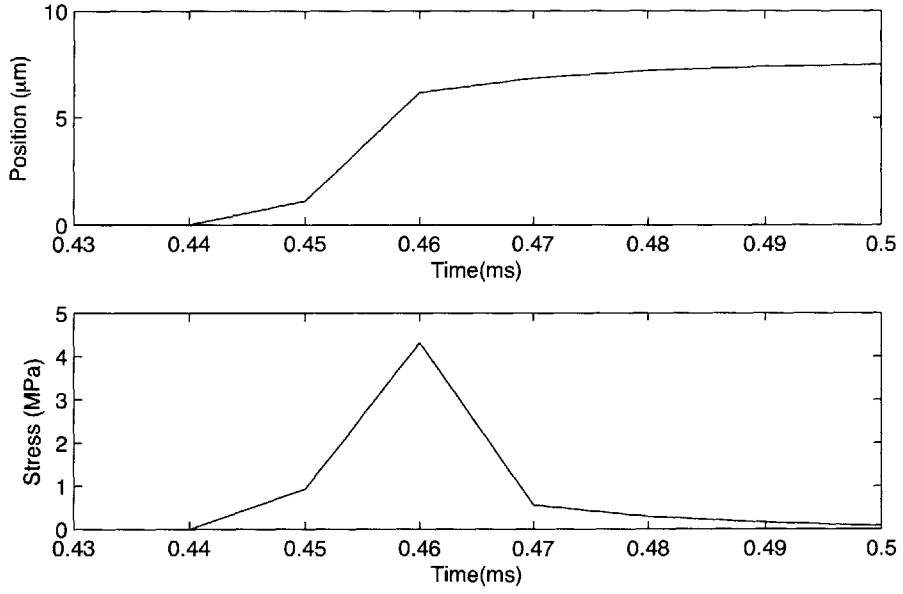

(b)

Figure 3-3: Typical pulse profile, showing (a) one full pulse, and (b) a magnified view of the fast rise portion of the pulse.

the stack has an infinite impedance compared to the FSMA, which is of course not true. Therefore, there will be a certain amount of rigid body motion accompanying the generated waves, which will tend to reduce the maximum stress. Other loss mechanisms such as viscous drag will reduce further the effective stress these pulses exert.

3.3 Testing Apparatus and Procedure

This section describes the apparatus used and the experiments performed to study acoustic actuation. In each case, a crystal that had been heat-treated and subjected to magnetic cycling was used. The performance of the crystals has been found to improve steadily over time, resulting in initial behavior that was not repeatable. For this reason, once assembled with the apparatus the crystals were conditioned by acoustic cycling, until their behavior became more consistent.

The adhesives used to bond the components of the apparatus should be chosen carefully based upon the type of stress that will occur at a particular interface. For bonds that will experience large shear stresses, the best choice is a two-part epoxy. Epoxy forms a thick bond line that is able to withstand high shear stresses. Where the maximum stress components are normal to the interface, a cyanoacrylate is the ideal adhesive, since it forms a thin bond line that relies on surface tension to keep the parts in intimate contact, thus transmitting normal stress components very effectively. In practice, the cyanoacrylate was often used, even where large shear stresses were expected, because it could be removed easily with acetone to allow modifications to the apparatus. This choice of adhesive led to occasional debonding between parts, which were then re-glued. A sharp decrease in performance was evident immediately before debonding, indicating that these bonds failed rapidly rather than gradually.

3.3.1 Dual Stack Configuration

For these experiments, two 33-mode piezoelectric stacks, oriented at 45 deg to the base of the crystal, were used. Figure 3-4 shows a schematic representation of the apparatus. As shown in Figure 3-4(a), the two stacks were bonded to a titanium triangular prism such that they were at an angle of 45 deg to the long axis of the crystal. Compressive pulses from

the stacks therefore had a maximum shear component parallel to the twinning planes of the crystal, which are horizontal in the figure. A steel reflector with a larger cross-sectional area than the crystal was affixed to the top of the crystal; since it has a higher impedance than the crystal, the incident and reflected waves will be of the same sign. The reflector was then joined by means of a flexible connector to a pushrod. A capacitive position sensor measured the displacement of a target at the end of the pushrod. Figure 3-4(b) shows a magnified view of the triangular prism. By elementary stress transformation laws, it may be seen that the compressive stress at the stack becomes a shear stress at the base of the crystal. This simple illustration neglects the effects of scattering from oblique incidence with the crystal wall, which could be significant, since stress waves scattered by an oblique interface undergo a change in both propagation and mode (e.g., longitudinal to shear), known as mode conversion.

The electrodes of the stacks were connected, as shown in Figure 3-2, to terminals $J10$, $J12$, and the power supplies adjusted such that the total voltage across both supplies was 100 V. By switching the relay, the active stack could be switched, allowing bi-directional actuation.

3.3.2 Single Stack Configuration

The first setup used to test the 15-mode stack is shown in Figure 3-5(a). This configuration included a titanium stepped-horn to act as a velocity transformer, and a reflector made of titanium rather than steel. The reflector was also given a sharply non-uniform cross-section, to increase dispersion of waves within it. Figure 3-5(b) shows the relationship between the motion of the stack and the resulting deformation of the FSMA. As may be seen, by the end of the pulse the tip of the crystal has moved in the opposite direction to the fast rise direction of the stack surface. Figure 3-6 shows a photograph of the apparatus. In Figure 3-6(a), the twin boundaries are clearly visible. The contrast betweeen variants was enhanced by using a directional light source and a polarized lens.

After initial experiments, a variation on the above apparatus was tested. Here, no horn was employed, the pushrod was eliminated and the reflector was changed to one made of steel. This reflector also had a larger cross-sectional area than the crystal, and was cylindrical to produce additional dispersion due to the change in shape. The steel reflector also had a

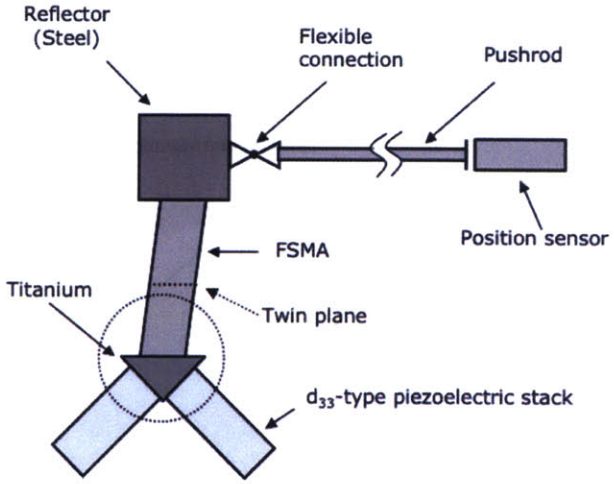

(a)

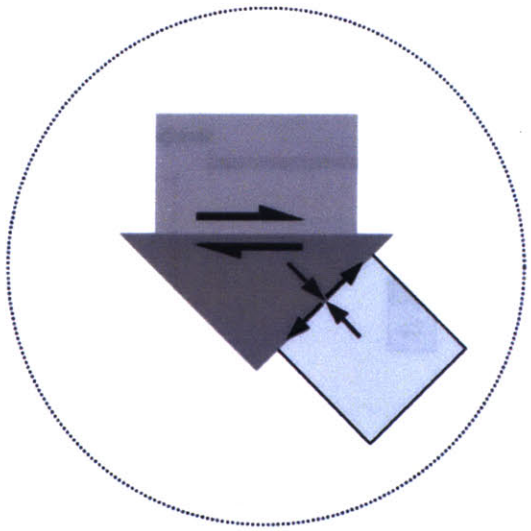

(b)

Figure 3-4: Dual stack configuration showing (a) the full assembly and (b) a schematic representation of the stress components resulting from longitudinal expansion of the stack.

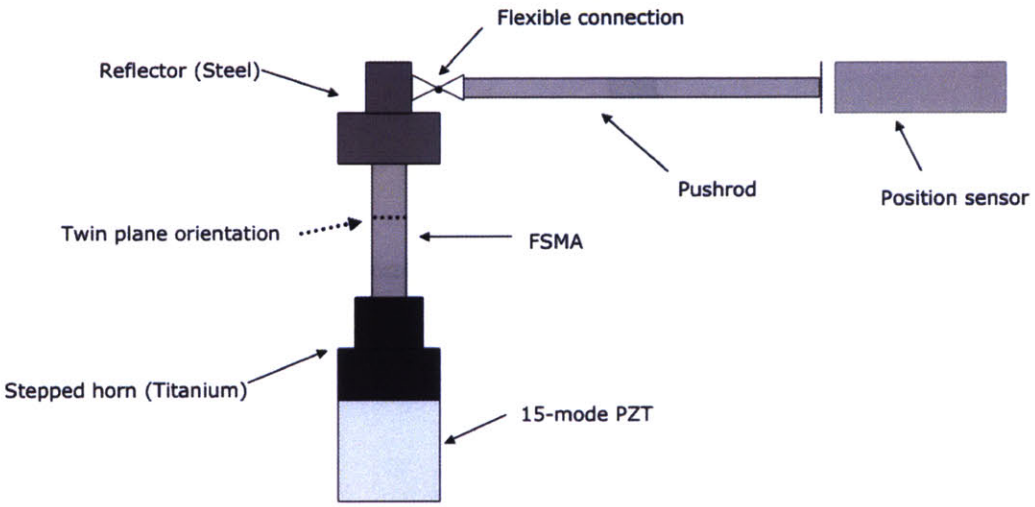

(a)

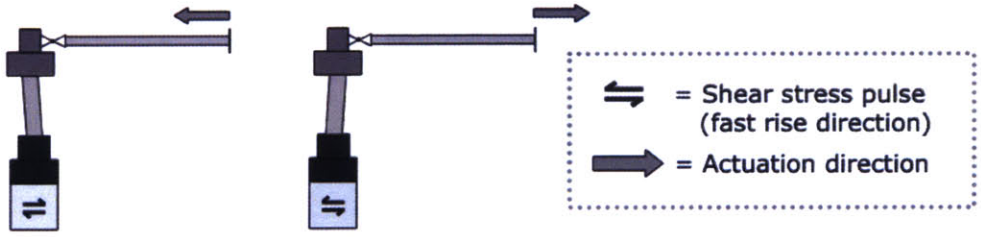

(b)

Figure 3-5: First setup used to test the 15-mode stack. (a) Schematic representation of the apparatus. (b) Illustration of the relationship between the pulse direction and the resulting deformation of the FSMA.

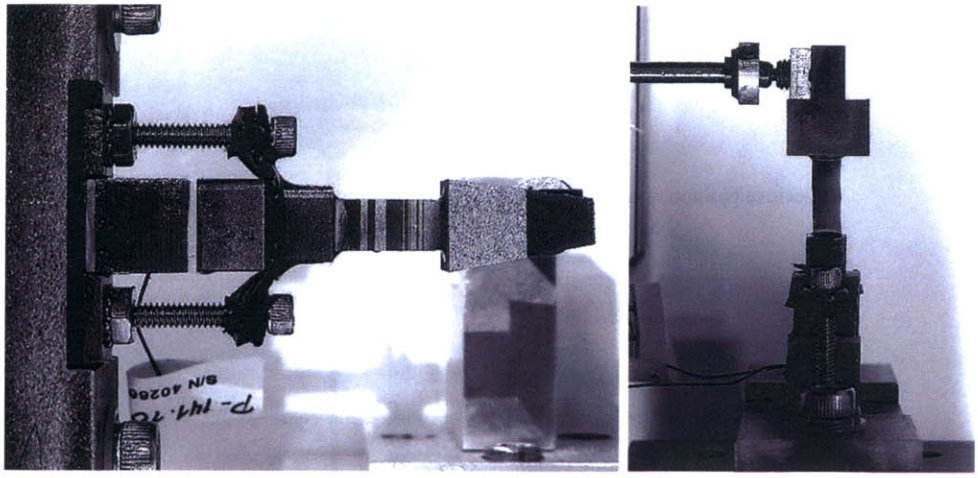

(a) (b)

Figure 3-6: Photographs of initial single stack configuration viewed from (a) the direction of actuation and (b) normal to the actuation direction.

higher impedance than the previous one, made of titanium, thus increasing the magnitude of the reflected stress waves, which would be of the same sign as the incident waves. The performance of the actuator improved after this change. The likely explanation is that the horn had a damping effect on the incident waves, due to the additional propagation distance, that was greater than any velocity amplification it may have produced. Typically, horns are employed to amplify longitudinal waves, which are non-dispersive. In the case of shear pulses, dispersion will decrease the maximum stress as the pulse propagates, counteracting the velocity-amplifying effect of the horn. Elimination of the pushrod prevented the crystal from being overly constrained in the event that the deformation was not well aligned with the rod. This apparatus was used for the remainder of the load-free actuation.

In order to test actuation against a load, the apparatus was modified as shown in Figure 3-7. Here, a right-angled rigid arm has been added to connect the reflector to a flexure, which exerts the loads. The arm was positioned such that the line of action of the force passes through the midpoint of the crystal. Without the arm, the load would exert a large bending moment at the base of the crystal. By shifting the load downward, this moment is split between the top and bottom ends of the crystal, giving two equal moments in opposite directions. This design allowed larger shear forces to be sustained while reducing the likelihood of debonding or fracture. A short length of stiff piano wire ensured that only axial

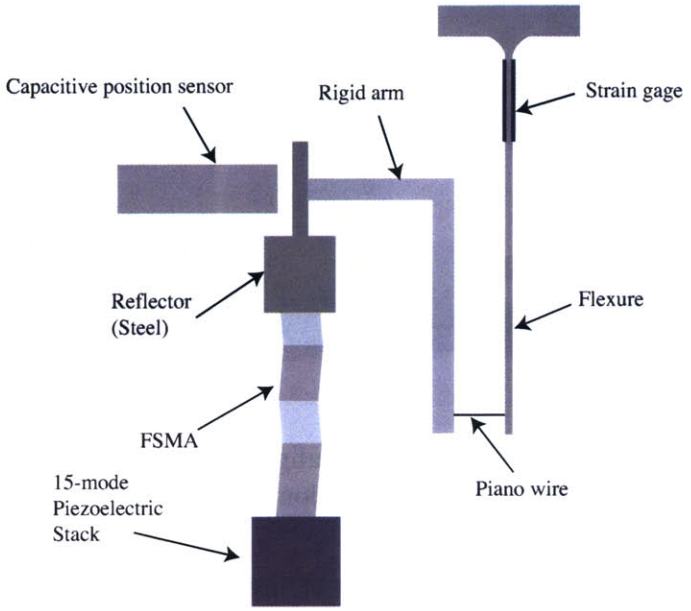

(a)

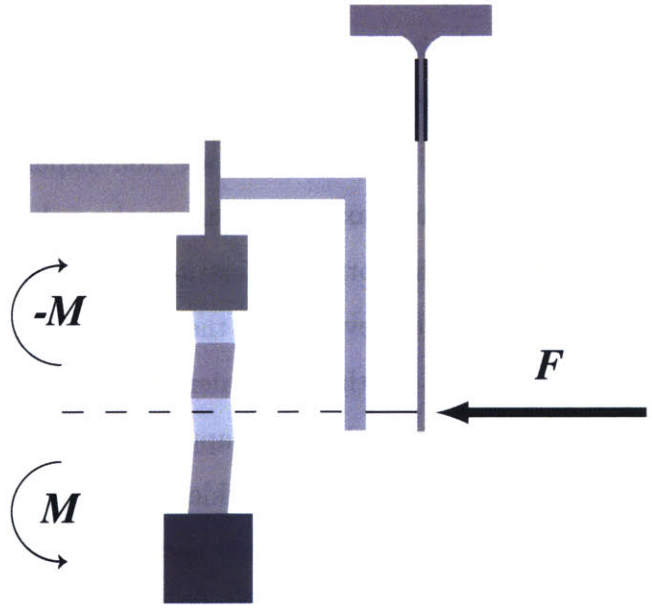

(b)

Figure 3-7: Apparatus used for actuation against a load showing (a) a schematic representation of the apparatus and (b) the bending moments induced by the load.

force components were transmitted. Strain gages at the base of the flexure were connected to a high-accuracy resistance meter, which allowed the deflection to be determined without the use of a Wheatstone bridge. To calibrate the flexure, it was mounted horizontally and calibration weights were suspended from the point where the force from the actuator would act.

To actuate against a load, the crystal was first pulsed to near its actuation limit in one direction. The sign of the pulses was then reversed, and an opposing prestress applied by moving the base of the flexure toward the crystal (in a horizontal direction with respect to the figure). The crystal was actuated against the load until no further displacement was observed. As the tip of the crystal moves toward the flexure, the opposing stress increases. This increase was typically on the order of 0.01 MPa, regardless of the prestress (since the force deflection relation for the flexure is linear). In order to examine the relationship between actuation and prestress, the average value during actuation was used.

Chapter 4

Results and Discussion

This chapter shows the results of the transverse mode, acoustic actuation experiments. For each experiment described in Chapter 3, the data will be presented, followed by a discussion of the significance of the results.

4.1 Dual Stack Configuration

In this experiment, described in Section 3.3.1, two longitudinal or 33-mode piezoelectric stacks are mounted at approximately 45 deg to the base of the crystal to produce shear pulses. The sample used for this experiment was cut, polished, and subjected to a thermomagnetic treatment as described in Chapter 3 in order to bias it in favor of the desired twinning system. The finished crystal had a length of 7.5 mm, and a cross-section of 7.3 mm $\times$ 6.2 mm. Here, the long dimension of the crystal is a $\langle 110 \rangle$ direction (the normal of the desired twin planes), while the longer and shorter dimensions of the cross-section are $\langle 100 \rangle$ and $\langle 110 \rangle$ directions, respectively. After heat treatment and extensive magnetic cycling, a portion of the crystal extending 5.4 mm from the base of the crystal was found to actuate readily. Above this line, twin boundaries lying at an angle to the desired, mobile twins were observed to have formed during the initial cooling from the austenite phase. These twins remained immobile throughout the magnetic training of the crystal, and could not be eliminated.

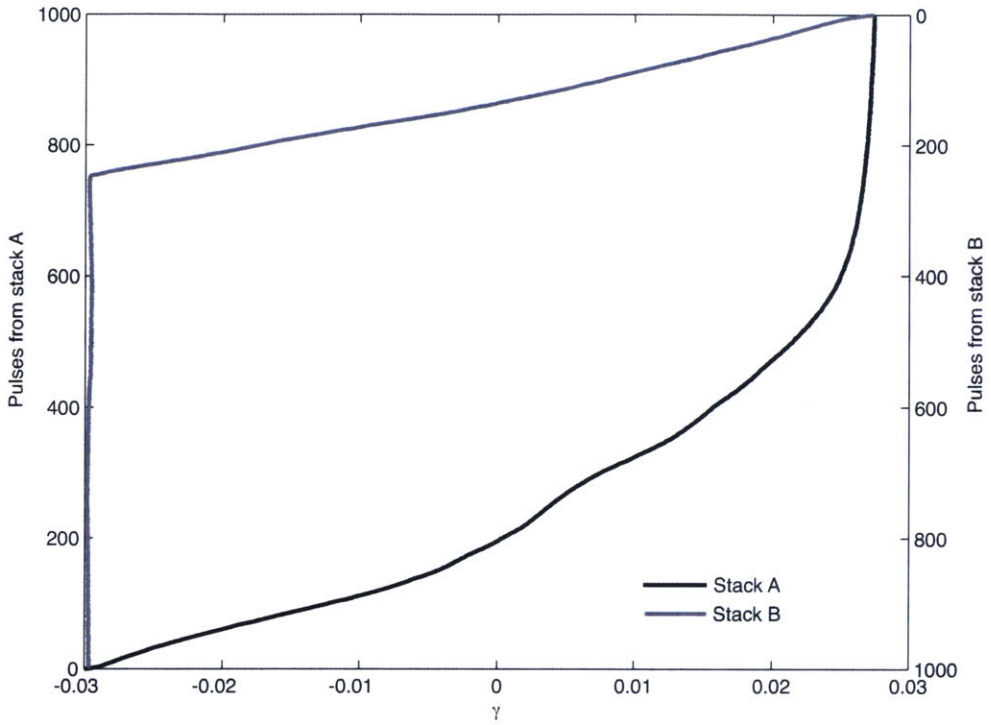

Figure 4-1: Number of 100 V pulses (f = 2 Hz) vs. strain for each 33-mode piezoelectric stack. Pulses from stack A produce a positive strain, while those from stack B give a negative strain.

4.1.1 Experimental Results

Despite the pinned region of the crystal described above, the application of 100 V pulses from the 33-mode piezoelectric stacks produced a complete transformation of the 5.4 mm active length of the crystal between variants. The data reported here give the strain γ relative to the total length of the crystal. If , instead, γ^* is the shear strain calculated with respect to the active length, $\gamma^* = 1.4\gamma$.

Figure 4-1 shows the result of the dual stack experiment, with the number of pulses plotted against the shear strain γ. The pulses reach the full amplitude of +100 V for these stacks, and the frequency is 2 Hz. In interpreting the plot, several details common to all plots of this format should be noted. First, in order to illustrate the loop-like nature of cyclic actuation, the pulses from stack B (represented by the gray curve) are plotted against the axis on the right hand side of the figure, which increases from top to bottom. The crystal is actuated to its limit using stack A, and the active stack is then switched to reverse the

actuation direction. Second, the horizontal position of the loop along the γ axis is somewhat arbitrary, and is determined generally as follows. For a given experiment, the total achievable strain of the crystal $\Delta\gamma_{max}$ is determined, and the limits defined as $\pm\frac{\Delta\gamma_{max}}{2}$. In other words, $\gamma = 0$ is the midpoint of the total displacement range that is attained in the experiment. Finally, the similarity between these plots and the stress-strain curve for a shape memory alloy may be noted. The slope of the curve indicates the stiffness, with twin boundary motion represented by a shallow slope (in a well conditioned crystal), and the actuation limit indicated by a sudden increase in stiffness.

As may be seen in Figure 4-1, transformation of the active region leads to a net actuation of $\Delta\gamma_{max}$= 7.7%. As explained above, this is with respect to the total length of the crystal. When calculated using the active length of 5.2 mm, the strain is found to be $\Delta\gamma^*_{max} = 10.6\%$, very close to the maximum theoretical value of 12%. A notable feature of the plot is its asymmetry. If the initial 250 pulses in each direction are compared, it may be seen that stack A produces an average displacement per pulse of 1.4 μm, while stack B produces an average displacement of 2.3 μm per pulse. Examining the entire range, 1000 pulses from stack A are required to produce the maximum strain, while this displacement is reversed in fewer than 200 pulses from stack B.

4.1.2 Discussion

The unequal response of the crystal to each stack may be due to a certain extent to properties of the crystal itself. In this case, the strain in the positive direction is limited by the intersection of the mobile twin boundaries with the incompatible, oblique twinning system. As the twin boundaries approach this pinning region, large strain fields leading to repulsive stresses. As the part of the crystal furthest from the pinning site is transformed entirely to the other variant, the only mobile twin boundaries will be those closest to this high-stress region. Consequently, there will be an increase in the slope of the curve.

A more important factor in this case, however, is most likely the unequal performance of the stacks themselves. As the crystal was cycled repeatedly, the performance of stack A continued to deteriorate. When the apparatus was disassembled, it was noticed that ceramic cover plate of stack A had cracked, parallel to the end face of the stack and approximately

1 mm below it. The crack surface indicated a brittle tensile failure, which was most likely due to the fact that no compressive prestress was applied to the stacks. Lead zirconate titanate is a very brittle piezoceramic that should not be subjected to excessive tensile stresses. Although the maxium rated voltage of the stacks was not exceeded, the rapid positive rise of the leading edge of the pulse could have led to an overshoot, and a consequent fracture in the stack.

Due to the likelihood of additional future stack failures in the absence of a compressive prestress, it was decided to suspend experiments using this configuration in favor of exploring the single-stack approach. The initial data are, however, encouraging: Given that the total stroke of the piezoelectric stack is approximately 14 μm, an average FSMA displacement of 2.3 μm per pulse represents 16% of the displacement of the stack, during each pulse, that is preserved as a net strain in the crystal. Thus, 100 pulses from the stack can produce a permanent strain in the FSMA that is approximately 16 times the maximum stroke of the stack.

4.2 Single Stack Configuration

4.2.1 Initial Acoustic Actuation without a Prestress

Preliminary tests of the single stack configuration, as described in Section 3.3.2, were carried out without an opposing or assisting shear stress. The crystal used had the same nominal composition as that used in the dual stack configuration, and was cut and polished to final dimensions of 12.5 mm $\times$ 5.8 mm $\times$ 4.3 mm ($\langle 110 \rangle \times \langle 100 \rangle \times \langle 110 \rangle$). Immediately following thermomagnetic treatment, only a small portion of the crystal (approximately $\frac{1}{6}$) was found to actuate; however no incompatible twin boundaries were observed as in the previous case. The twinning stress soon after treatment was measured quasi-statically, and found to be approximately 1.8 MPa. These experiments began by using a titanium stepped horn and titanium reflector. Eventually, the horn was eliminated and the reflector replaced with one made of steel.

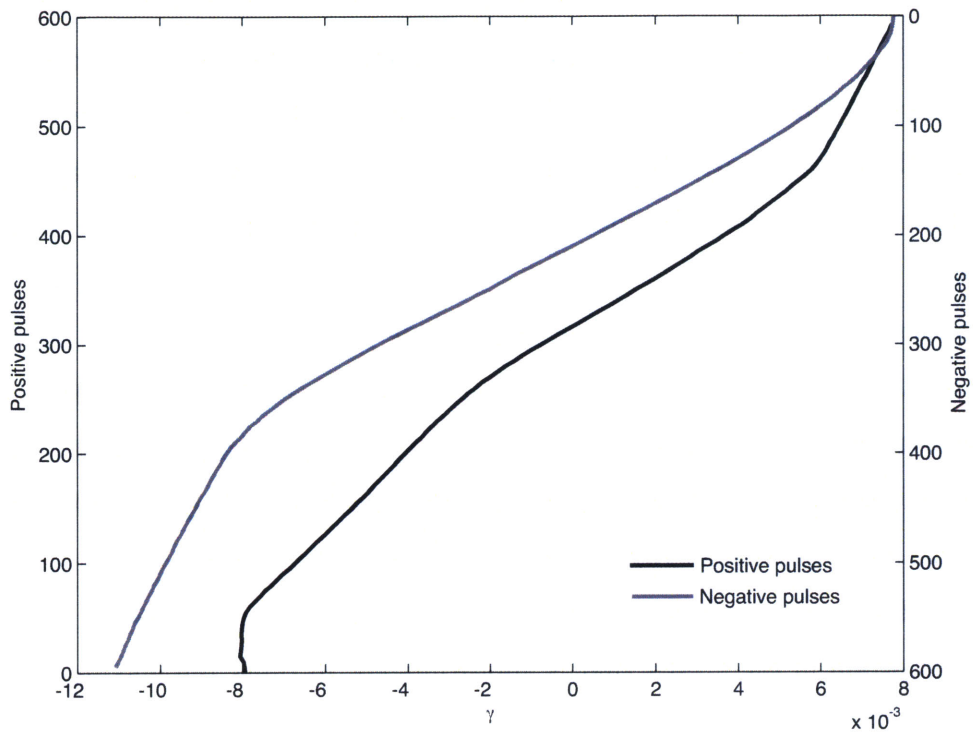

Figure 4-2: Early strain loop using ±500 V pulses from a single 15-mode piezoelectric stack. Total strain is only approximately 2%, but is increasing gradually over time. Here, the crystal undergoes an increase in the maximum absolute negative strain over the course of the loop.

4.2.1.1 Experimental Results

Figure 4-2 illustrates the effect of acoustic conditioning, showing a strain loop taken soon after thermomagnetic treatment, using ±500 V pulses. The poorly conditioned crystal exhibits only a modest shear strain of approximately 2%, with an average displacement of the FSMA per pulse of approximately 0.4 μm. However, as the figure shows, the displacement range is observed to increase with each cycle. The starting point of the loop represents the largest negative strain that had been obtained until that point; however, over the course of a single loop the maximum strain in the negative direction increases from -0.8% to -1.1%.

After about 100 cycles, the crystal exibited approximately 5% shear strain. At this point, it was decided to remove the titanium stepped horn, and to replace the titanium reflector with one made of steel. Prior to affixing the steel reflector, however, the apparatus was tested without a reflector. Interestingly, the half of the crystal closest to the stack was observed to

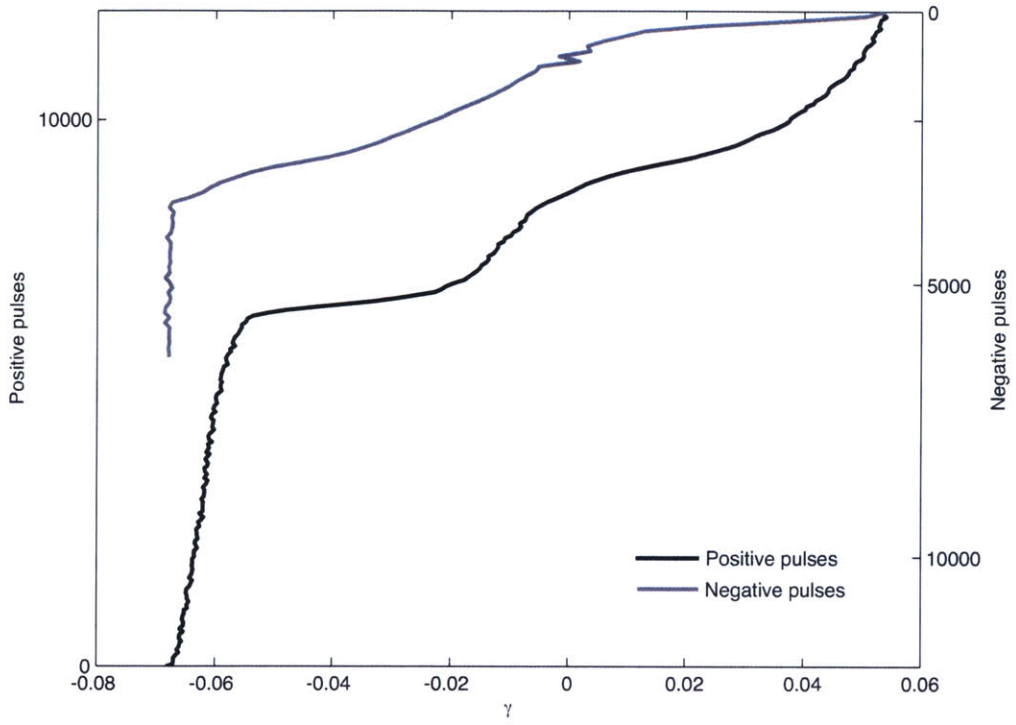

Figure 4-3: Early loop with 100 Hz, ±500 V pulses, showing full 12% shear strain.

transform completely to the desired variant, while the half closest to the free end transformed into the opposite variant.

When the horn was removed and the reflector was changed, the displacement began to increase appreciably. After a further 100 cycles, the total shear strain increased to the full 12% expected for this composition. The slope of the curves remained irregular, however, as shown in Figure 4-3. During the initial 6000 positive pulses, the crystal had a high effective stiffness, becoming much softer after this point. It was observed that during the stiff region of the curve, very few mobile twin boundaries could be seen. Because the total velocity of the tip of the crystal is the cumulative velocity of all the twin boundaries, a small number of mobile boundaries leads to a smaller strain rate. To avoid sweeping out all the twin boundaries, therefore, the pulse polarity was switched immediately before it achieved the second, single variant state (represented by $\gamma = +6\%$). In this manner, several discrete twins were retained, resulting in a much more rapid initial actuation in the opposite direction.

Figure 4-4 shows still frames taken of the crystal duing an actuation cycle soon after the full crystal became active. The images illustrate the non-uniformity and inconsistent behavior observed during initial training. The images correspond to a crystal which is initially at $\gamma \simeq -6\%$, subjected to positive 500 V pulses. In this case, the initial state contains some very thin twins, not visible in the image, because the crystal had not been pulsed into a purely single-variant state prior to actuation. Within the first three seconds of actuation, the thin twins close to the stack expand rapidly, so that by the time 10 seconds have elapsed approximately 60% of the crystal has transformed. It requires a further 70 seconds to actuate the remaining 40%. As described above, it may be seen that during this period of slow actuation, the only twin boundary that appears to be mobile separates the large twinned region at the left of the crystal from the untwinned region near the reflector.

As the sample is actuated further, the region near the reflector is observed to become less mobile, until a region at that end would no longer transform between variants. In addition to this immobile region, a debonding event resulted in the crystal landing on its corner, while bearing the mass of the heavy reflector. The impact produced a triangular region at the corner containing an incompatible twinning system, further reducing the mobile range. Where this incompatibly-twinned region interects the mobile region a crack has developed, approximately 1.5 mm in length, which has not been observed to propagate during cycling but rather to open and close as the crystal is actuated.

After extensive training, the crystal actuated readily between γ =-3% and $\gamma = \cdot 3\%$, but did not exceed this range. Figure 4-5 illustrates the behavior of the crystal following training. In Figure 4-5(a), the result of actuating up to the two limits of the range is illustrated. The response has become much more symmetric, with the actuation rate decreasing as the limits are approached. Figure 4-5(b) shows the result of actuating within the range without approaching the limits. Here, the behavior is almost linear and symmetric. To illustrate the repeatability of the behavior in this range, the strain is plotted against the number of pulses of either type as the actuator is switched between the two directions.

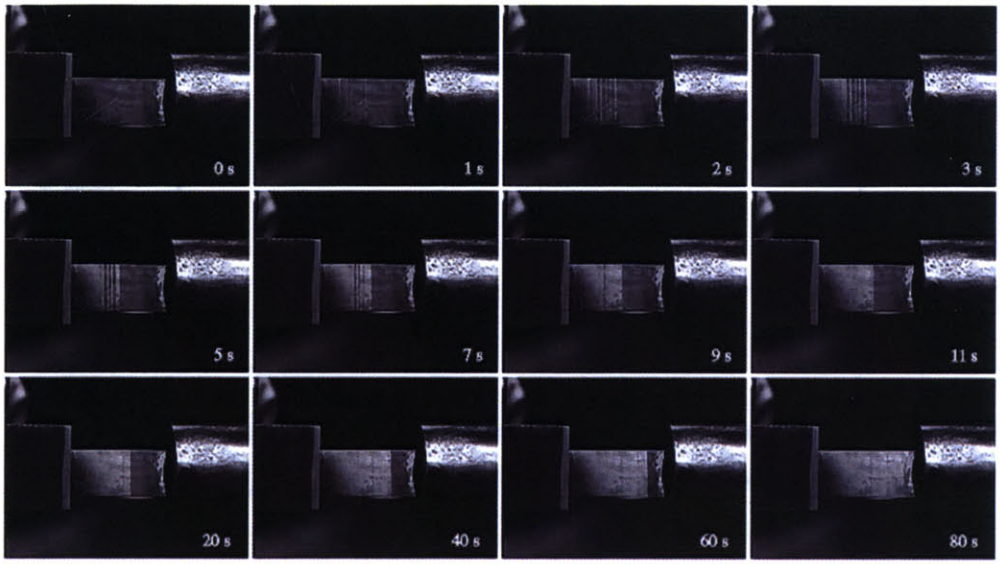

(a) Side view, showing the transformation between variants at various moments in time. The displacement is out of the plane of the page.

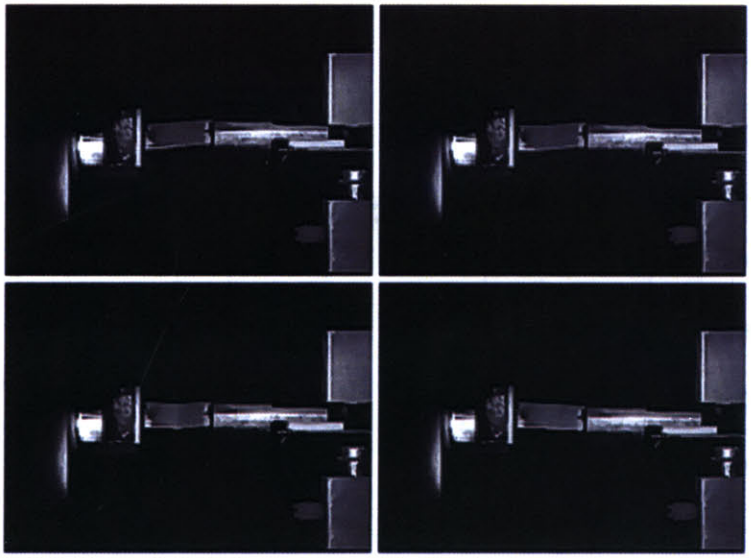

(b) Top view of crystal at four points during actuation.

Figure 4-4: Still images from video taken of full 12% actuation. To enhance the contrast between variants, a directional light source and polarized lens were used.

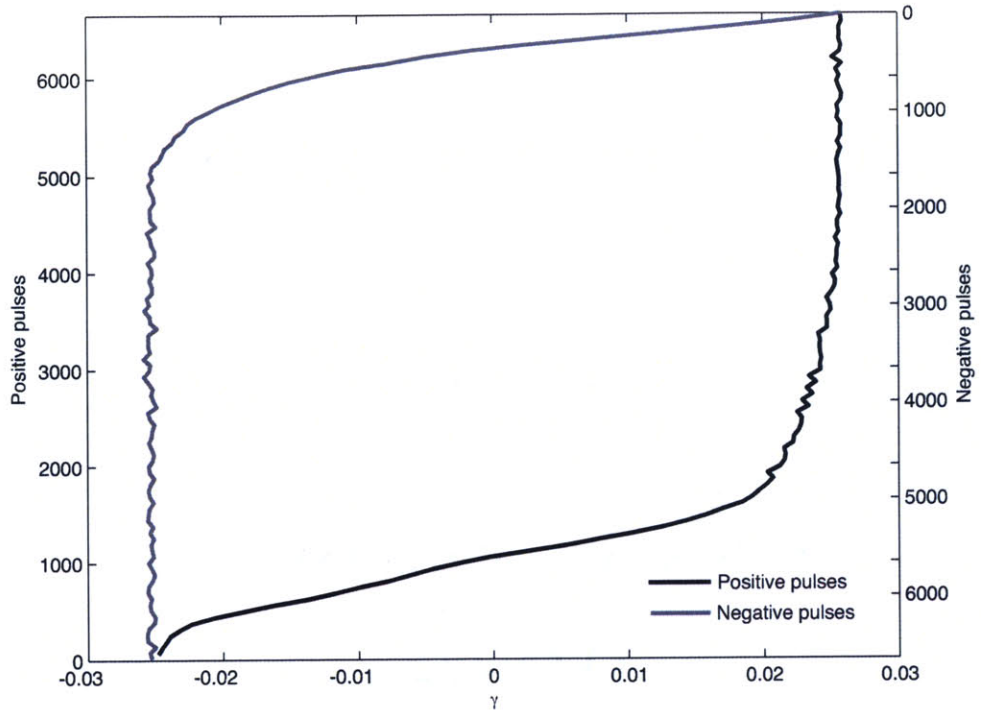

(a) 500 V, 100 Hz actuation loop for fully trained crystal, between range limits.

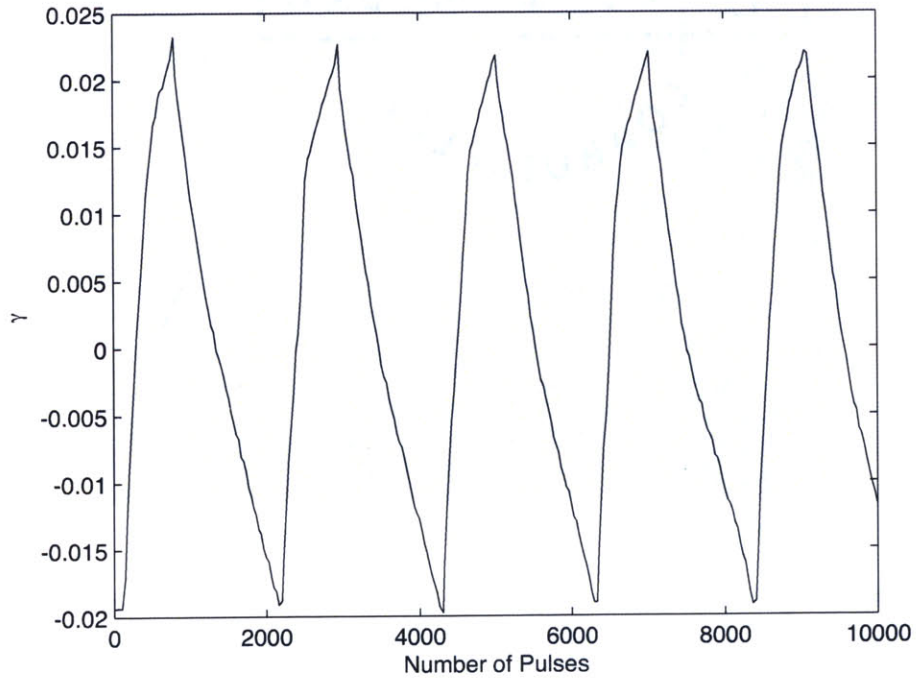

(b) 500 V, 60 Hz quasi-linear actuation within range limits.

Figure 4-5: Post-training behavior using single 15-mode stack.

4.2.1.2 Discussion

The improvement in performance of the actuator over the course of the experiment may be attributed both to modifications to the apparatus, and progressive conditioning of the crystal. Replacing the titanium reflector with one made of steel, and eliminating the horn were observed to improve performance. As explained in Chapter 3 the higher impedance of the steel reflector (vs. one made of titanium) is expected to increase the magnitude of the reflected stress waves, which will be of the same sign as the incident pulses, because the reflector has a higher impedance than the crystal. The observation that, when the reflector is removed, only the half of the crystal closest to the piezoelectric stack will actuate, is consistent with the expectation that, in the absence of a reflector with a larger acoustic impedance than the crystal, the reflected stress waves will be inverted and will tend to induce a shear in the opposite direction. Furthermore, as is also noted in Chapter 3, horns are inappropriate for use as velocity transformers when the waves are dispersive. Because dispersive waves decrease in amplitude as they propagate, any potential benefit of using the stepped horn as a velocity transformer is mitigated by the additional attenuation it produces.

Conditioning the crystal, on the other hand, improves actuation by increasing twin boundary mobility. When a twin boundary becomes pinned at an obstacle, or defect in the microstructure, a certain critical stress is necessary to overcome this obstacle. The stochastic nature of these pinning events and the resulting non-uniformity in twin-boundary motion has been well documented [16]. In addition to the distribution in pinning strengths, the variation in behavior from cycle to cycle may depend on the size and distribution of the twins themselves. As explained in Chapter 2, as two twins approach each other a repulsive stress field develops between them [23] . This stress hinders the ability of additional twinning disconnections to move the edge of the crystal, and hence the ability of the twin boundary to propagate. Equation 2.5 shows that the stress necessary to grow the twin is inversely proportional to the twin thickness. As thin twins are forced together to become thicker twins, they become more mobile. Therefore, the overall mobility of the crystal depends on not only the distribution of obstacles, which is unlikely to change significantly over time, but the distribution in location and thickness of the twins at a given moment in time. In acoustic

actuation, unlike the magnetic or mechanical cases, twin boundary motion is probably localized to the immediate vicinity of the pulse. Thus, the likelihood of the crystal deforming in an identical manner during each cycle, with the same twin boundaries moving in the same order, is even less than when a global state of stress is induced. For this reason, acoustic actuation tends to be less repeatable than, say, magnetic actuation of these materials.

The number of twin boundaries moving at a particular time have the greatest effect on the overall actuation speed. It has been observed that the motion of twin boundaries that already exist is more likely to occur than the nucleation of new boundaries. By remaining within the actuation range, a number of discrete twins may be retained in the crystal; this leads to a more even response when the actuation direction is switched.

Finally, the observation of cracks that form at twin-intersection points is consistent with a phenomenon described by Müllner [23] and explained in greater detail in Chapter 2. When twinning dislocations move to the edge of single crystal in an ordinary, mobile twin, they form a disconnection wall; the twin boundary is visible on the crystal face, and the deformation is stable. Similarly, where twins intersect, twinning dislocations in each twin cannot move past the intersection point due to the discontinuity in the lattice. It is possible that disconnection walls could form at the interface, which are associated with large stress fields that can lead to fracture at wall. If all elements of disconnection motion are reversible, however, as disconnections move away from the wall, the wall dissolves and the crack closes. With repeated actuation, some deformations may become irreversible, though, and in this case the crack can grow. It is thus expected that this crack will eventually lead to the brittle failure of the crystal.

4.2.2 Frequency Dependence

Once the behavior of the device had become relatively consistent and repeatable, the first effect to be tested was the dependence of actuation rate on the pulse frequency or repetition rate. Due to limitations of the driver circuit, investigation was restricted to the 20 to 200 Hz range.

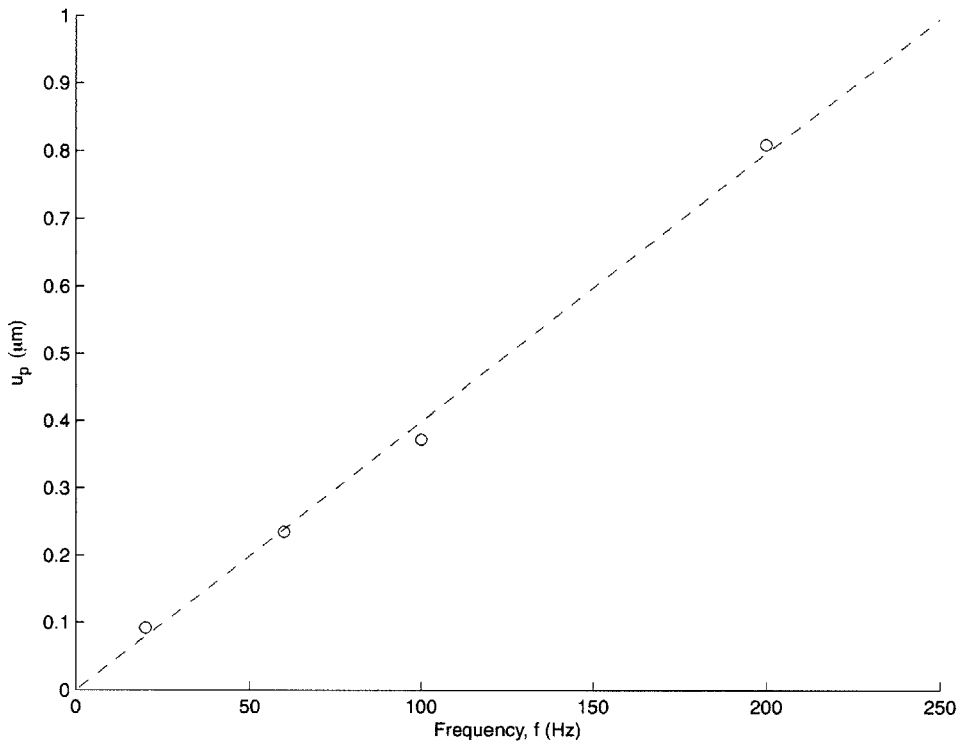

Figure 4-6: Average displacement of the FSMA per pulse, u_p vs. frequency, f. A linear fit to the data, $u_p = \left(3.98 \times 10^{-3} \frac{\mu m}{Hz}\right) \times f$, is also plotted.

4.2.2.1 Experimental Results

Figure 4-6 shows the results of this experiment, in which the stack generates ±500 V pulses at various frequencies. Here, the rise time of the pulse is held constant, while the trailing edge of the pulse is adjusted to discharge the stack in time to produce the next pulse. In order to make meaningful comparisons, the most consistent section of each curve, where it appears nearly linear, was measured.

As may be seen, there is a marked increase in the average displacement of the FSMA per pulse with increasing frequency. A linear fit to the data,

$$u_p = \left(3.98 \times 10^{-3} \frac{\mu m}{Hz}\right) \times f, \tag{4.1}$$

shows that this increase is apparently linear. While an increase in actuation rate per unit

time is expected due to the higher pulse frequency, the increase in the displacement per pulse was not anticipated. The result of the increase in the strain per pulse with frequency is that the increase in the strain per unit time will be quadratic with respect to the frequency. It appears that as long as the rise time is much shorter than the fall time ($t_r \ll t_f$), optimum performance is achieved when the frequency is maximized.

4.2.2.2 Discussion

If the pulse frequency were increased into the kHz range, it is expected that there would be a decrease in the actuation strain per pulse as $t_f \rightarrow t_r$. The increase in the strain per pulse with frequency, at the frequencies investigated here, is more difficult to explain. A possible explanation could be constructive interference between reflected pulses and subsequent outgoing pulses. As they become closer together, there is a greater chance that one pulse will overlap with the reflection of another to create a larger net stress.

Because these waves are known to be dispersive, however, and the time between pulses is so large compared with the time required for them to propagate through the crystal, interference between the pulses is unlikely. Rather, this effect is more likely to arise from the mass inertia of the crystal, which can cause twin boundary motion to persist after the initial peak stress pulse has passed. Additional experiments are needed to determine the fraction of the total pulse time that twin boundary motion occurs, and the optimum pulse frequency for actuation.

4.2.3 Actuating against a Load

Using a flexure, as described in Chapter 3, the crystal was actuated by driving the stack at a pulse frequency of 100 Hz, and a pulse voltages of $\pm$500 V, against an opposing force. The direction of actuation was then switched such that the force assisted in actuation. The convention adopted here is that the shear stress τ against which the crystal actuates is considered negative if it opposes actuation and positive if it assists.

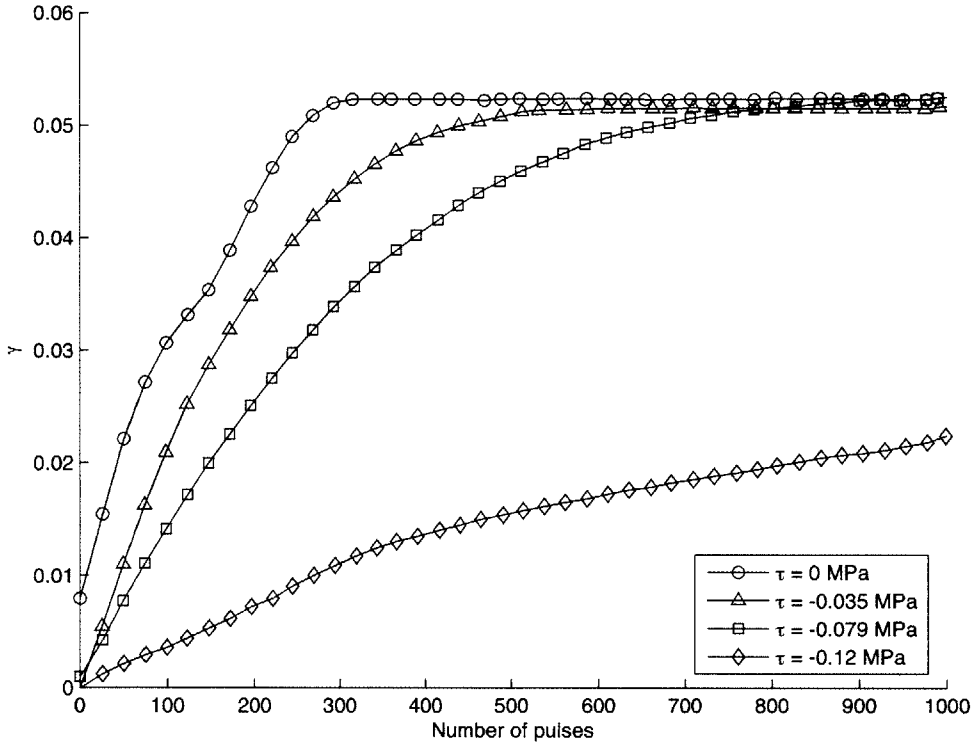

Figure 4-7: Actuation against an opposing stress, $\tau < 0$.

4.2.3.1 Experimental Results

The displacement curves produced while actuating against an opposing stress are shown in Figure 4-7. Here, it may be seen that, as the opposing shear stress increases, there is a decrease in the slope of the displacement curve. The maximum strain produced after 1000 pulses, however, remains constant for $\tau = 0$, -3.5×10^{-2}, MPa and -7.9×10^{-2} MPa. As the load increases to $\tau = -1.2 \times 10^{-1}$ MPa, there is a reduction not only in the rate of strain, but in the maximum strain as well.

In order to compare these curves in a more quantitative manner, the average displacement per pulse u_p is calculated using the number of pulses required to reach 75% of the total strain at that load. Because the experiments are carried out at a constant frequency, the displacement per pulse is proportional to the velocity of the tip of the crysta. The results are plotted in Figure 4-8. A linear fit is also plotted and agrees well with the data. By

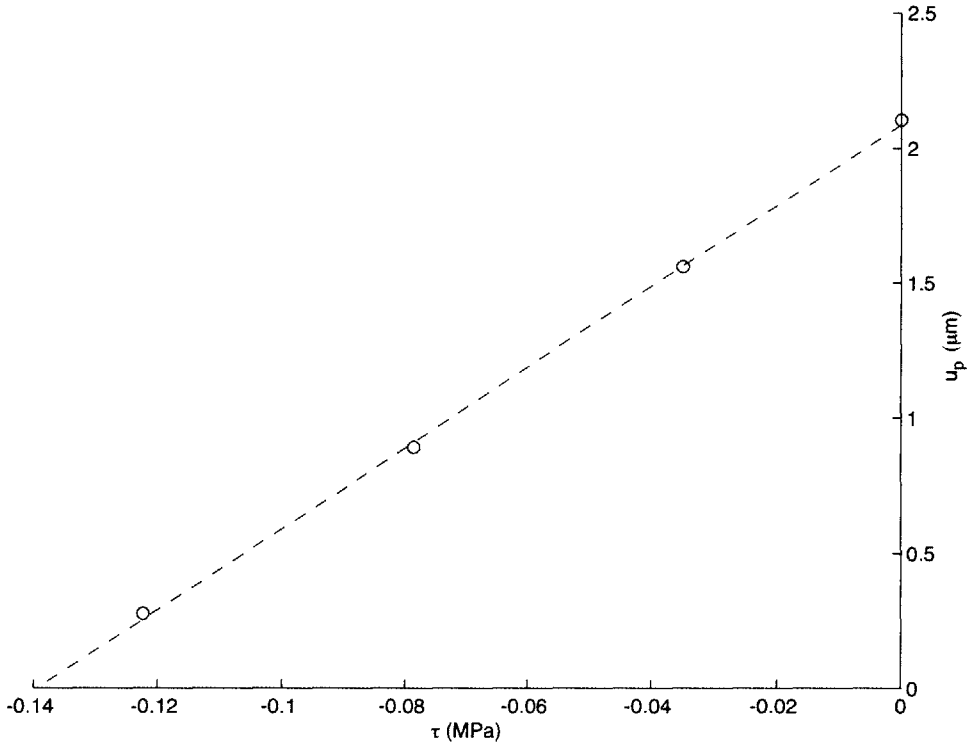

Figure 4-8: Average displacement per pulse u_p vs. opposing shear stress. A linear fit to the data, $u_p = \left(15\,\frac{\mu\text{m}}{\text{MPa}}\right) \times \tau\,\mu\text{m}$, is also plotted.

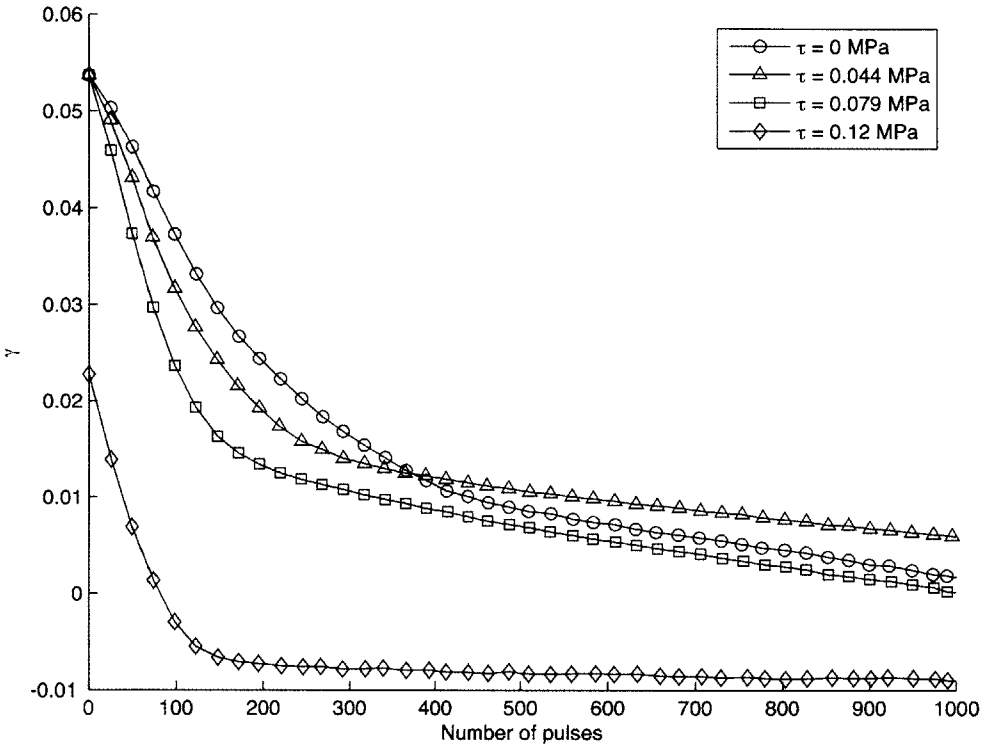

Figure 4-9: Actuation with an assisting shear stress $\tau > 0$.

projecting to $u_p = 0$, it may be determined that the approximate blocking stress is $\tau_{pre} = -1.4 \times 10^{-1}$ MPa. It should be noted that the blocking stress is not equal to the twinning stress, but rather the difference between the acoustic stress and the twinning stress. If the total induced stress driving twin boundary motion is given by

$$\tau_{\text{induced}} = \tau_{\text{acoustic}} - \tau_{\text{pre}}, \tag{4.2}$$

it may be deduced that $\tau_{\text{acoustic}} \simeq \tau_0 + 1.4 \times 10^{-1}$ MPa, where τ_0 is the threshold twinning stress. When $\tau_{\text{pre}} < -1.4 \times 10^{-1}$ MPa, $\tau_{\text{induced}} < \tau_0$, and twin boundary motion cannot take place.

The results of actuating with an assisting load are shown in Figure 4-9. Here, again, when $\tau_{\text{pre}} = 0$, 4.4×10^{-2} MPa and 7.9×10^{-2} MPa, the maximum strain remains approximately constant. When the load is increased to $\tau_{\text{pre}} = 1.2 \times 10^{-1}$ MPa, however, the crystal is able

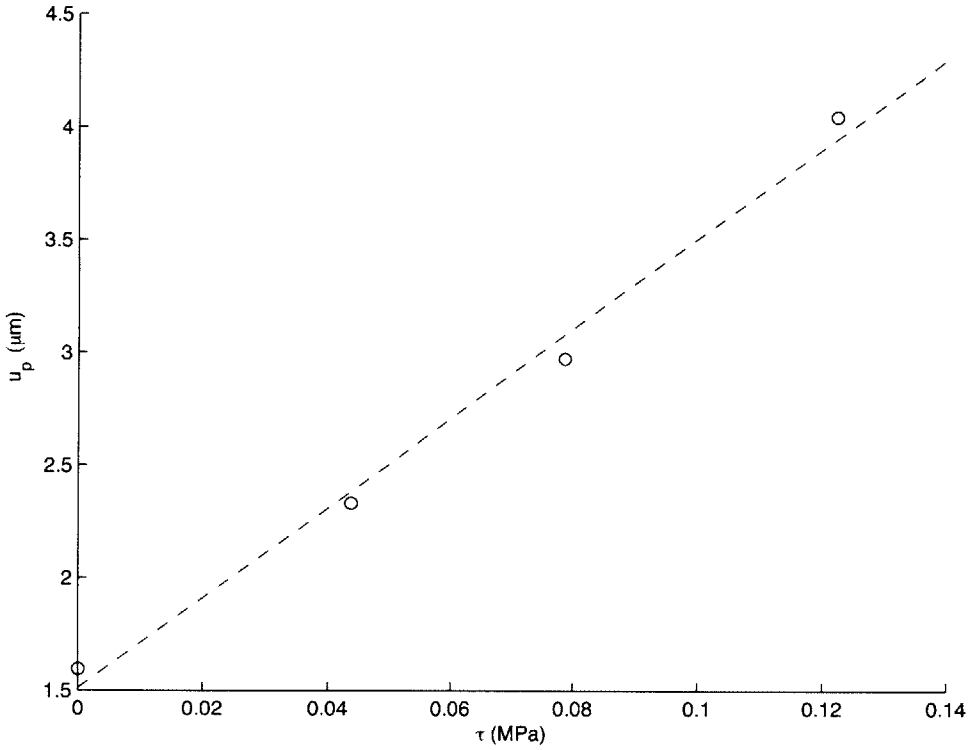

Figure 4-10: Average displacement per pulse u_p vs. assisting shear stress. A linear fit to the data, $u_p = \left(20\,\frac{\mu\text{m}}{\text{MPa}}\right) \times \tau + 2.1\mu\text{m}$, is also plotted.

to transform beyond the initial limit. When the average displacement per pulse is calculated in the same manner as for the opposing load case, and the values are plotted, the result is shown in Figure 4-10.

The equations of the linear fits to the data from the opposing and assisting load cases were

$$u_p = \left(15\,\frac{\mu\text{m}}{\text{MPa}}\right) \times \tau + 2.1\mu\text{m} \quad , \quad \tau_{\text{pre}} < 0, \tag{4.3}$$

and

$$u_p = \left(20\,\frac{\mu\text{m}}{\text{MPa}}\right) \times \tau + 2.1\mu\text{m} \quad , \quad \tau_{\text{pre}} > 0, \tag{4.4}$$

Equations 4.3 and 4.4 agree quite well with one another. The discrepancy between the

slopes shows a slight difference in actuation behavior between the two actuation directions. Although this actuator design performs more symmetrically than the dual stack configuration, small differences in actuation performance between the two directions seem to be inevitable. In this case, the opposing and assisting load tests are carried out in opposite directions. Therefore, at the beginning of the assisting load test, the crystal is in one variant state, while for the opposing load case the crystal is initially at the opposite end of its range. The average displacement per pulse at zero load for the two tests, $u_p = 1.9\,\mu$m, is significantly greater the approximately 0.4 μm that was measured at 100 Hz in the load-free configuration.

4.2.3.2 Discussion

For a given opposing stress, the total strain that can be achieved is determined by the strongest obstacles to twin boundary motion. There are three possible cases. First, if the total induced stress, as calculated according to Equation 4.2, is greater than the stress required to overcome the strongest obstacle, full actuation may be achieved. Second, if the induced stress lies between the strengths of the weakest and strongest obstacles, some but not all twin boundaries may be mobile. In this regime, there will be a reduction in the total strain as well as a decrease in slope, as in the curve in Figure 4-7 corresponding to $\tau_{\mathrm{pre}} = -1.2 \times 10^{-1}$ MPa. Finally, when the induced stress falls below the strength of the weakest obstacle, no actuation can take place.

The more interesting effect of the applied stress is on strain rate. The linear relationship between the two appears to show evidence of a viscous loss mechanism, similar to that observed for plastic dislocation motion. If the total induced stress acting on a twin boundary exceeds the twinning stress, the additional energy goes into the motion of the twin boundary. Various loss mechanisms, including internal friction and domain wall motion, can produce a viscous effect, where the motion of the twin boundary generates an opposing force that is proportional to its velocity. Eventually, the opposing force equals the driving force, and a terminal velocity is reached.

Because in both the opposing and assisting cases the stress produced by the stack remains constant, while the prestress is changed, the slope of the resulting plot is directly related to

the dependence of the rate of strain on the applied stress. As explained in Section 2.3.2, the crystalline drag coefficient B may be calculated based on the slope of this line according to Equation 2.26, if the time during which twin boundary motion takes place during each pulse, t_p, is known. In practice, determining t_p is very difficult. Furthermore, as the results in Section 4.2.2 show, the time of twin boundary motion appears to be related to the pulse frequency. Expressed in terms of this time, however, an approximate expression of

$$B = \left(6 \times 10^8 \frac{\mathrm{N}}{\mathrm{m}^2}\right) \times t_p, \tag{4.5}$$

is obtained. For example, if twin boundary motion takes place only during the time that the pulse exceeds the twinning stress, which is on the order of 5 μs, one obtains a value for B on the order of 100 Ns/m^2. A typical value for dislocation motion in aluminum is 5×10^{-5} Ns/m^2 [13], seven orders of magnitude below this value. However, it is noted that plastic dislocations move with speeds that of hundreds of meters per second, while twin boundaries appear to move at approximately 0.1 m/s, so clearly these effects are on a different scale. For a twin boundary to move, the entire cross section of the crystal must transform. Due to the large cross-sectional area of the twin plane, large numbers of defects may contribute to the apparent viscocity. Also, twin boundary motion is known to be a highly dissipative process, as shown by Feuchtwanger [7] by the use of Ni–Mn–Ga in energy damping composites. Many polymers, which are also used for damping, have viscosities greater than 1000 Ns/m^2. Therefore, it is possible that the value obtained here for twin boundary motion is reasonable.

Several other observations are of interest. The asymmetry in the response of the actuator between the two actuation directions may come from two sources. Crystal properties may play a role in this behavior. For example, if the actuation limit in one direction is imposed by incompatible twinning systems, the crystal may appear to be stiffer when it approaches this state than if the crystal were able to transform completely. Asymmetries in the bonding of the crystal to the stack and reflector, and in the actuation apparatus itself, are likely to play an even more important role.

Also, it is notable that there is a considerable improvement in the performance of the

actuator when the flexure apparatus is used. The increase in strain rate may be the result of the additional mass added to the reflector in the form of the flexure and connector. The additional components would aid to disperse any waves transmitted into them, further mitigating the effect of the inverted waves that would be reflected from the free end of the reflector. It may be seen that, for the largest assisting load tested here, the average displacement per pulse is over 4 μm. In this case, since the stack has a stroke of approximately 7.5 μm, this displacement constitutes around 53% of the stack stroke that is retained in the FSMA for each pulse.

From Figure 4-7, the output energy density of the actuator may be calculated for the various loads. If the actuator exerts a force F over a distance Δx, the total work W done by the actuator is given by

$$W = F\Delta x. \tag{4.6}$$

Then, if the crystal has a cross-sectional area A and length l, the volumetric energy density E will be given by

$$E = \frac{W}{Al} = \left(\frac{F}{A}\right)\left(\frac{\Delta x}{l}\right) = \tau_{pre}\gamma. \tag{4.7}$$

Thus, the output energy density may be calculated simply as the product of the prestress and the total strain. Examining Figure 4-7, the maximum energy density corresponds to an opposing prestress of 8×10^{-2} MPa, and is equal to approximately 4000 J/m^3.

The average power output during the initial part of the displacement curve may be estimated from Figure 4-8. At 8×10^{-2} MPa, the average displacement per pulse is about 0.8 μm. The work done in actuating this distance against the load is 1.6 μJ, which gives an average mechanical power over the 0.01 s duration of the pulse of $P_m = 0.16$ mW.

The average electrical power consumption of the piezoelectric stack is given by

$$P_e = \frac{CV^2}{2t}, \tag{4.8}$$

where C is the capacitance of the stack, V is the total voltage to which it is charged, and t is the time between pulses. For the 15-mode stack, $P_e = 375$ mW, which gives an overall

actuator efficiency of

$$\eta = \frac{P_m}{P_e} = 4 \times 10^{-4}. \tag{4.9}$$

Chapter 5

Conclusions

5.1 Acoustic Actuation

The work presented here builds upon that of Chambers *et al.* [4, 3] in proving the viability of a purely acoustic method of actuating shape memory alloys, particularly the ferromagnetic shape memory alloys of the Ni–Mn–Ga system. With no prestress, shear strains of up to 5% have been realized in as little as 2.5 s at a pulse repetition rate of 100 Hz, using a single 15-mode piezoelectric stack. Over 3% strain was observed to occur within the first second, which is equivalent to an average displacement of 1.5–2.0 μm per pulse during that time. By applying an assisting static prestress of 0.12 MPa, the displacement of the FSMA per pulse reaches over 4 μm, which is 53% of the stroke of the piezoelectric stack.

Actuation against an opposing load has also been demonstrated, with the maximum blocking stress of -0.14 MPa in this case indicating that the stress pulses generated exceed the twinning stress by approximately this amount. Given an approximate twinning stress of 1.8 MPa for this crystal, the effective acoustic stress is therefore approximately 1.9 MPa. This estimate is consistent with the calculated upper bound for the magnitude of the stress pulses, which, based on linear elastic wave theory, is found to be approximately 4 MPa. Due to non-elastic losses and rigid body motion of the crystal, the actual stress is expected to be less than this value.

The limit on actuation stress is due to the stroke and rise-time of the stack and pulse profile used here. By generating a higher material velocity at the stack-crystal interface,

higher stresses could be achieved, and therefore larger loads could be actuated against. In order for the deformation to remain after the pulse has passed, however, the opposing stress cannot exceed the twinning stress.

When the maximum mechanical work done by the actuator against a load is compared with the electrical power consumption, we obtain an overall efficiency of only about 4×10^{-4}. Clearly, this value is very low, which would likely limit the utility of this technology where efficiency is important. Similarly, the low blocking stress makes this type of actuator unsuitable for applications requiring actuation against large loads.

The potential attractiveness of this design lies in the large strains that can be obtained with a solid state actuator (i.e., without requiring a stroke amplification mechanism), and the fact that the strain is semi-permanent after the pulses have passed. This "set-and-forget" behavior could make this technology suitable for certain micropositioning applications. The large strains that FSMAs can produce would give displacements about two orders of magnitude greater than those that could be achieved with similary-sized piezoelectric devices.

Moreover, typical piezoelectric micropositioning devices require that a particular voltage be maintained in order to maintain a particular position. The longer the displacement, and hence voltage, must be held, the more an acoustically actuated device becomes attractive.

5.2 Transverse Mode vs. Longitudinal Mode Actuation

Based on the results of Chambers *et al.*, where longitudinal actuation was investigated, it can be calculated that the 1% strain obtained in approximately 1 s (at 100 Hz) is equivalent to about 1 μm per pulse, because the crystal had a length of 10 mm. It should be noted that an equal displacement would occur in the transverse direction, due to the 45 deg angle of the twin boundaries in this configuration. The resulting total displacement is $\sqrt{2}\,\mu$m, of which only 1 μm was exploited. Therefore, the total displacement per pulse was very similar to that observed here for the no-load case.

Several differences are worth noting. First, the stack used here had a total stroke of approximately 7.5 μm when operating dynamically, while the 33-mode stacks used for longitudinal actuation were measured to give a pulse displacement of approximately 15 μm.

Thus, in this respect, the transverse configuration results in a larger fraction of the stack stroke being conserved as a plastic strain in the crystal.

Also, because the longitudinal stacks have a much higher capacitance than the 15-mode stacks (1600 nF vs. 30 nF), they consume more power. At 100 Hz and the maximum rated voltages for each stack, the 33-mode stacks require about 800 mW, while the 15-mode devices consume about 375 mW.

The Chambers actuator has a smaller crystal volume, smaller total displacement, and the displacement is not purely in the actuation direction. These factors combine to give it a an average mechanical power against a 100 kPa load of approximately 0.07 mW, which is less than half the approximately 0.2 mW produced by the transverse mode actuator. It also requires more electrical power, so its overall efficiency of about 2×10^{-4} is half that of the transverse mode device.

Another advantage to the transverse mode actuator is its smaller form-factor, because the clamp may be dispensed with. Also, whereas the Chambers actuator performed better in compression than in tension, this design allows equally effective actuation in each direction.

5.3 New observations

Several observations from these experiments indicate phenomena that are not well-described in the existing literature. In particular, the results indicate the presence of a viscous loss mechanism, which limits the rate of strain that can be produced by a given stress. In previous work (e.g., [15, 3]), the idealized stress-strain behavior was described as shown in Figure 5-1. Here, the effective stiffness of the crystal while twin boundary motion is taking place is represented as the constant c_{tb}. An estimate of this value is given as 30 ± 20 MPa [3]. This representation neglects the effect of the stress on the strain rate, however. If Figure 5-1 is understood as the quasi-static stress-strain curve, the implication of the non-zero slope during twin boundary motion is that, if a stress greater than σ_0 is applied, a discrete strain is obtained.

In contradiction to this theory, in these experiments there existed a wide range of opposing stresses against which the maximum total strain did not change. This effect may be noted

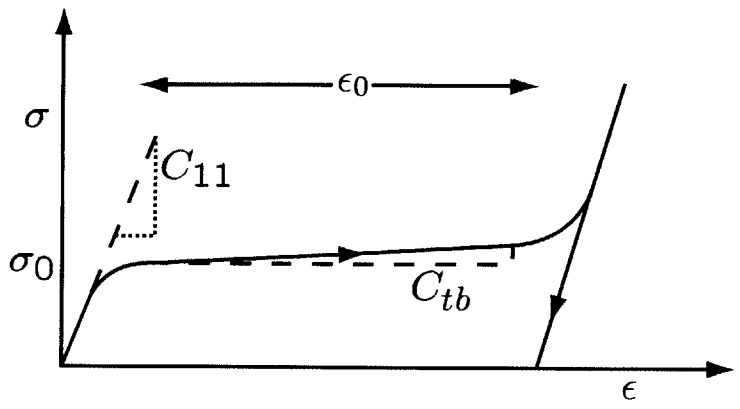

Figure 5-1: Idealized stress-strain behavior of an FSMA, as represented in earlier research. From [3].

in Figures 4-7 and 4-9. Only as this opposing stress approached the threshold for twin boundary motion did the total strain begin to decrease. In other words, a curve of the type shown in Figure 5-1 is representative not of the quasi-static stress-strain behavior, but of the deformation at a particular strain rate. The effect of the applied stress on the rate of strain was observed in these experiments to be significant, with a linear relationship between the two.

In some earlier experiments (e.g., [4, 3]), the actuation load did appear to have an effect on the total strain. A possible explanation is that the distribution of defect strengths is much narrower in the experiments presented here. A reduction in the range of pinning strengths could be the result of improved material processing, which could reduce the number of types and range of strengths of any defects. Thus, a given stress $\tau > \tau_0$ in the newer crystals would cause a larger proportion of the mobile twin boundaries to move. It is therefore possible that a sufficiently large applied stress could cause all mobile twin boundaries to move in the new crystals, while in the older material many twin boundaries would have pinning strengths much larger than the applied stress.

The dependence of the rate of strain on the applied stress, and the linear nature of that relationship, require further study before they are well understood. Factors such as internal friction and domain wall motion may play a part. The large apparent viscosity when compared to plastic dislocation motion may be a result of the fact that, in order for a

twin boundary to move through a single crystal, it must extend over the entire cross-section. Thus, as the twin boundary progresses it must overcome all of the defects in its plane, which could act to increase the viscosity associated with twin boundary motion.

Another interesting observation pertains to the increase in the strain per pulse with increasing frequency. This effect was not anticipated, and indicates that there is an interaction between adjacent pulses that becomes more beneficial as the pulses get closer together. Because the time taken for a pulse to traverse the crystal is far less than the time between pulses, and since these pulses are known to be dispersive and thus will be attenuated over time, it is unlikely that this effect is due to the constructive interference of incident and reflected pulses. Rather, it is more likely due to the inertia of the crystal, which could cause twin boundary motion to persist after the pulse has passed. The effect of inertia on twin boundary motion is another area that warrants further study.

5.4 Future work

As explained above, the dependence of strain rate on the applied stress is an area that certainly merits in-depth investigation. The results of these experiments appear to show a viscous loss mechanism that leads to a linear relationship between the two. By gaining a better understanding of the viscoelastic properties of this material, a far more accurate constitutive relation can be obtained, which would allow actuators utilizing these materials to be modeled more accurately.

In order to investigate the dynamic stress-strain behavior, a purely mechanical method would be more suitable. An attractive experiment would be to subject the ends of a {100}-cut crystal to a precisely-controlled, rate-dependent, longitudinal strain, and to measure the uniaxial stress simultaneously. The theoretical maximum velocity for twin boundary motion is the plastic wave speed, if there are no other intrinsic limits to the speed of twin boundary motion. Such high-strain-rate experiments would be particularly challenging, and would likely require the use of a projectile to produce a sufficiently large material velocity in the crystal.

Although purely acoustic actuation may prove to be of limited utility, the principles

explored here may be useful in designing magnetic-acoustic actuators that would combine an applied magnetic field with an acoustic stress to induce actuation. One such method is the acoustically-assisted actuator discussed in Section 1.2.2, which employs a varying magnetic field and a constant acoustic signal. An alternative could be to use a stationary magnetic field, just below the threshold field, and to apply a sinusoidal acoustic stress that would cause the threshold to be exceeded in one direction, but not in the other.

As interest in active materials continues to grow, new types of material and methods of actuation will certainly be discovered. The intriguing properties of Ni–Mn–Ga, the variety of ways in which it can be actuated, and the feasibility of using a purely acoustic method for materials with low twinning stresses, hint at the significant, untapped potential for development in this field.

Bibliography

[1] Rajeev Ahluwalia, Turab Lookman, and Avadh Saxena. Dynamic strain loading of cubic to tetragonal martensites. *Acta Materialia*, 54:2109 2120, 2006.

[2] A. D. Bozhko, A. N. Vasil'ev, V. V. Khovaĭlo, I. E. Dikshteĭn, V. V. Koledov, S. M. Seletskiĭ, A. A. Tulaĭkova, A. A. Cherechukin, V. G. Shavrov, and V. D. Buchel'nikov. Magnetic and structural phase transformations in the shape-memory ferromagnetic alloys $Ni_{2+x}Mn_{1-x}Ga$. *Journal of Experimental and Theoretical Physics*, 88(5):954–962, May 1999.

[3] Joshua M. Chambers. Design and characterization of acoustic pulse shape memory alloy actuators. Master's thesis, Massachusetts Institute of Technology, 2005.

[4] Joshua M. Chambers, Steven R. Hall, and Robert C. O'Handley. Characterization of piezoelectrically induced actuation of Ni–Mn–Ga single crystalsi–mn–ga single crystals. In William D. Armstrong, editor, *Smart Structures and Materials*, volume 5761, pages 478–489, 2005.

[5] Thomas H. Courtney. *Mechanical Behavior of Materials*. McGraw-Hill Higher Education, 2000.

[6] Liyang Dai, Jun Chui, and Manfred Wuttig. Elasticity of austenitic and martensitic NiMnGa. In Dimitris C. Lagoudas, editor, *Proceedings of SPIE*, volume 5053, pages 595–602, 2003.

[7] Jorge Feuchtwanger, Sadie Michael, Jiankang Juang, David Bono, Robert C. O'Handley, Samuel M. Allen, and Catherine Jenkins. Energy absorption in Ni–Mn–Ga-polymer composites. *Journal of Applied Physics*, 93(10):8528–8530, May 2003.

[8] Karl F. Graff. *Wave Motion in Elastic Solids*. Dover Publications, Inc., 1975.

[9] Christopher P. Henry. *Dynamic Actuation Properties of Ni–Mn–Ga*. PhD thesis, Massachusetts Institute of Technology, May 2002.

[10] Christopher P. Henry, Jorge Feuchtwanger, David Bono, Miguel Marioni, Pablo G. Tello, Marc Richard, Samuel M. Allen, and Robert C. O'Handley. AC performance and modeling of ferromagnetic shape memory alloy actuators. In Christopher S. Lynch, editor, *Proceedings of SPIE*, volume 4333, pages 151–161, 2001.

[11] J. E. Huber, N. A. Fleck, and M. F. Ashby. The selection of mechanical actuators based on performance indices. In *Proceedings of the Royal Society A: Mathematical, Physical and Engineering Sciences*, volume 453, pages 2185–2205, 1997.

[12] Physik Instrumente. Catalog: P-111 – P-151, 2006.

[13] J. N. Johnson and L. M. Barker. Dislocation dynamics and steady plastic wave profiles in 6061-T6 aluminum. *Journal of Applied Physics*, 40(11):4321–4334, October 1969.

[14] E. H. Lee. Some recently developed aspects of plastic wave analysis. In Julius Miklowitz, editor, *Wave Propagation in Solids*, 1969.

[15] Miguel A. Marioni. *Pulsed magnetic field-induced twin boundary motion in Ni–Mn–Ga*. PhD thesis, Massachusetts Institute of Technology, 2003.

[16] Miguel A. Marioni, Samuel M. Allen, and Robert C. O'Handley. Nonuniform twin-boundary motion in Ni–Mn–Ga single crystals. *Applied Physics Letters*, 84(20):4071–4073, 2004.

[17] Miguel A. Marioni, Robert C. O'Handley, and Samuel M. Allen. Pulsed magnetic field-induced actuation of Ni–Mn–Ga single crystals. *Applied Physics Letters*, 83(19):3966–3968, 2003.

[18] V. V. Martynov and V. V. Kokorin. The crystal structure of thermally- and stress-induced martensites in Ni_2MnGa single crystals. *Journal de Physique III France*, 2:739–749, 1992.

[19] C. C. Mei. Unpublished lecture notes. Massachusetts Institute of Technology, 2004.

[20] P. Müllner, V. A. Chernenko, and G. Kostorz. A microscopic approach to the magnetic-field-induced deformation of martensite (magnetoplasticity). *Journal of Magnetism and Magnetic Materials*, 267:325–334, 2003.

[21] P. Müllner, V. A. Chernenko, and G. Kostorz. Large cyclic magnetic-field-induced deformation in orthorhombic ($14M$) Ni–Mn–Ga martensite. *Journal of Applied Physics*, 95(3):1531–1535, February 2004.

[22] P. Müllner and C. Solenthaler. A proper model of a deformation twin for twin-intersection problems. *Philosophical Magazine Letters*, 69:111–113, 1994.

[23] Peter Müllner, Debashis Mukherji, Myriam Aguirre, Rolf Erni, and Gernot Kostorz. Micromechanics of magnetic-field-induced twin-boundary motion in Ni–Mn–Ga magnetic shape-memory alloys. *Solid-to-Solid Phase Transformation in Inorganic Materials*, 2:171–185, 2005.

[24] S. J. Murray, M. Marioni, S. M. Allen, and R. C. O'Handley. 6% magnetic-field-induced strain by twin boundary motion in ferromagnetic Ni–Mn–Ga. *Applied Physics Letters*, 77(6):886–888, August 2000.

[25] S. J. Murray, M. A. Marioni, A. M Kukla, J. Robinson, R. C. O'Handley, and S. M. Allen. Large field induced strain in single crystalline Ni–Mn–Ga ferromagnetic shape memory alloy. *Journal of Applied Physics*, 87(9):5774–5776, 2000.

[26] R. C. O'Handley. Model for strain and magnetization in magnetic shape-memory alloys. *Journal of Applied Physics*, 83(6):3263–3270, March 1998.

[27] R. C. O'Handley, S. J. Murray, M. Marioni, H. Nembach, and S. M. Allen. Phenomenology of giant magnetic-field-induced strain in ferromagnetic shape-memory materials (invited). *Journal of Applied Physics*, 87(9):4712–4717, May 2000.

[28] Bradley W. Peterson, Jorge Feuchtwanger, Joshua M. Chambers, David Bono, Steven R. Hall, Samuel M. Allen, and Robert C. O'Handley. Acoustic assisted, field-induced strain in ferromagnetic shape memory alloys. *Journal of Applied Physics*, 95(11):6963–6964, June 2004.

[29] M. Richard, J. Feuchtwanger, D. Schlagel, T. Lograsso, S. M. Allen, and R. C. O'Handley. Crystal structure and transformation behavior of Ni–Mn–Ga martensites. *Scripta Materialia*, 54:1797–1801, 2006.

[30] Marc Richard. Unpublished research. Massachusetts Institute of Technology, 2005.

[31] Marc Louis Richard. *Systematic analysis of the crystal structure, chemical ordering, and microstructure of Ni–Mn–Ga ferromagnetic shape memory alloys*. PhD thesis, Massachusetts Institute of Technology, 2005.

[32] A. Sozinov, A. A. Likhachev, N. Lanska, and K. Ullakko. Giant magnetic-field-induced strain in NiMnGa seven-layered martensitic phase. *Applied Physics Letters*, 80(10):1746–1748, March 2002.

[33] Marcelo Stipcich, Lluís Mañosa, and Antoni Planes. Elastic constants of Ni–Mn–Ga magnetic shape memory alloys. *Physical Review B*, 70(054115), 2004.

[34] Piezo Systems. Catalog: Low voltage piezoelectric stacks, 2006.

[35] K. Ullakko, J. K. Huang, C. Kantner, and R. C. O'Handley. Large magnetic-field-induced strains in Ni_2MnGa single crystals. *Applied Physics Letters*, 69(13):1966–1968, September 1996.

7387-32